



University of Bremen

Alfred Wegener Institute - Helmholtz Centre for Polar and
Marine Research

MASTER THESIS

**Heat and hydrological extremes in warm
climates:
Lessons from paleoclimate simulations**

Author:

Ahmadreza Masoum

Anagraphic data:

Shiraz (IR), 21.09.1985

Matriculation Number:

3130946

First Examiner:

Prof. Dr. Gerrit Lohmann

Second Examiner:

Dr. Martin Werner

Supervisor:

Dr. Christian Stepanek

September 2020

Declaration of copyright

Hereby I declare that my Master's Thesis was written without external support and that I did not use any other sources and auxiliary means than those quoted. All statements which are literally or analogously taken from other publications have been identified as quotations and citations.

Declaration with regard to publishing theses

I agree that for research purposes third parties can use my thesis stored in the University archive.

Bremen / September 2020

Ahmadreza Masoum

Abstract

Extreme climate events and their impacts are currently arising as a critical feature of climate change. Paleoclimate studies are essential for understanding global environmental change and predicting extreme's trends as the paleo-studies determine the factors that caused changes in the climate. Many studies have suggested that the mid-Pliocene and last interglacial (LIG) can be potentially used as an analogue for the future climates, but the extreme climate events are often missing in these studies. This thesis aims to show whether the LIG and mid-Pliocene are considered as analogues for the future of two extreme climate indices, including summer days index and heavy precipitation index. The MPI-ESM and COSMOS are employed to simulate the LIG, mid-Pliocene, pre-industrial, and future climates. First, the anomalies of temperature, precipitation, and selected indices are plotted for the simulations with respect to PI. In general, the summer days and heavy precipitation patterns are similar to the temperature and precipitation patterns, respectively. The probability density functions of climate variables and extreme indices in the centre of North America and Africa, the south of Africa, and Malaysia, clearly show that the increases in the average temperature and precipitation result in a growth in the corresponding extreme index. Comparing the anomaly plots for different simulations, the LIG can be only considered as analogue for future of summer days index in the northern-hemisphere regions such as the centre of North America. The mid-Pliocene not only is a good analogue for the summer days at the global scale but also can be used regionally for the prediction of heavy precipitation events. Due to the different characteristics of models employed in this project, there are some discrepancies in the results of similar simulations produced by MPI-ESM and COSMOS.

Contents

1	Introduction	5
2	Data and Methods	10
2.1	MPI-ESM-1-2-LR	10
2.2	COSMOS	12
2.3	Experimental Design	13
2.3.1	MPI-ESM-1-2-LR Setup	14
2.3.2	COSMOS Setup	16
2.4	The Climate Data Operators (CDO)	18
2.5	Climate Extreme Indices	18
2.6	T-Test Analysis for Comparing Climate Anomalies	22
2.7	Kolmogorov–Smirnov Test	23
3	Simulated Mean Climate and Extremes	25
3.1	MPI-ESM	25
3.1.1	Surface Temperature	25
3.1.2	Precipitation	26
3.1.3	Climate Extreme Indices	27
3.2	COSMOS	32
3.2.1	Surface Temperature	32
3.2.2	Precipitation	33
3.2.3	Climate Extreme Indices	33
4	Climate Extremes via Analysis of PDF	42
4.1	MPI-ESM	42

4.2	COSMOS	47
5	Discussion	52
5.1	Climate extreme indices at global scale	52
5.2	Last Interglacial	53
5.3	Mid-Pliocene	55
5.4	MPI-ESM vs COSMOS	57
6	Conclusions	60
	Acronyms	63
	References	64
A	MPI-ESM vs COSMOS	71

Chapter 1

Introduction

Climate change poses fundamental questions in climate research, among them: How did the global climate change in the past, and what are the determining factors that caused these changes? In which manner has human activity affected the global environment and how can these impacts be distinguished from natural variability? What are the natural limits (e.g., in the frequency of events, trends, extremes) of the global environment, and how are changes in the boundary conditions (e.g., greenhouse gases, ice extent) impacting on this natural environment? What are the vital forcing factors (e.g., greenhouse gases, orbital forcing, volcanic aerosols) and how will they dominate climate change on societal timescales (season to century)? To answer these questions, it is imperative to carry out paleo-climate research ([Council, 1999](#)). Paleo-climate studies, particularly for warmer climates of the past, can be implemented to learn for future climate and environmental change. One phenomenon, which is coveted to be predicted as it is able to influence directly on human life, is climate extreme. Extremes are commonly defined in two forms. In disciplines of climate change research, extremes generally refer to rare events within the statistical reference distribution of particular variables (e.g., temperature, precipitation) at a particular place, and thus to the tails of the probability density function (PDF; [Klein Tank et al., 2002](#); Fig. 1.1). This statistical definition of extremes is also assumed in this thesis. In the second definition, extremes can be explained in terms of hazardous weather resulting in drastically adverse impacts on ecosystems, human safety and health, water management, agriculture,

energy, insurance, tourism and transport (Klein Tank et al., 2002). Consequently, the severity of an event depends on the historical climate record, the biological system, and whether the ecological level of interest focuses on the physiology of individuals, population, or structure of communities or ecosystems (Jenouvrier et al., 2015). Climate extremes can arise from external forcing of the climate system, such as from increasing greenhouse gases, natural variability, and some combination of the two (Easterling et al., 2016).

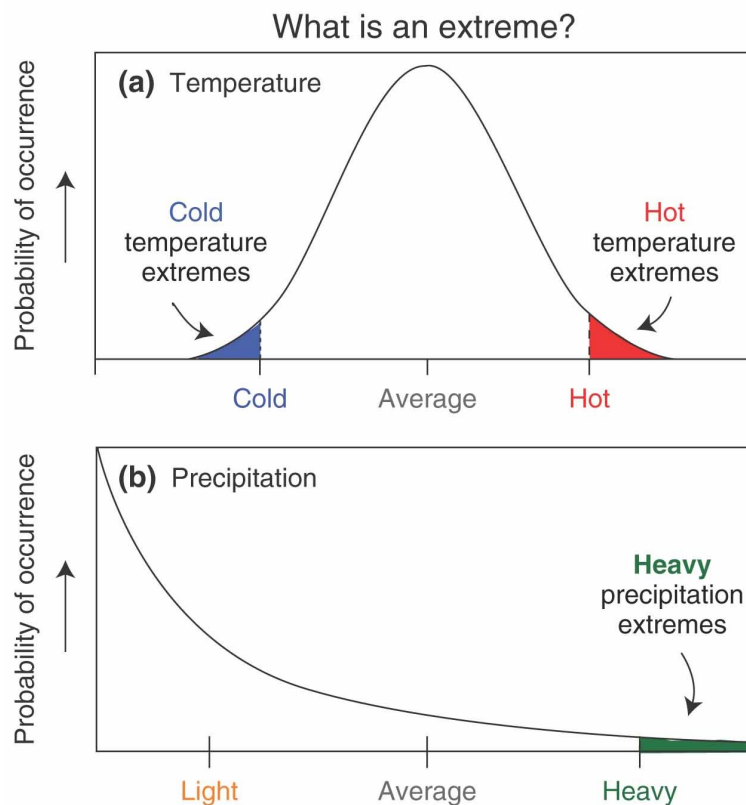


Figure 1.1: Schematic of the probability distributions of daily temperature and precipitation. The higher the black line, the more often weather with those specific characteristics occurs. Extremes are denoted by the shaded areas (Zhang et al., 2011).

During the past few decades, increased attention has been paid to extreme weather and climate events due to the often massive loss of human life and rising costs associated with them (Meehl et al., 2000). It is thought that some of these extremes are becoming more frequent, and the main reason for that is anthropogenic activities (Trenberth et al., 2015) such as greenhouse gas and aerosol emissions (Planton et al., 2008). Plenty of studies have been published on a particular aspect of cli-

mate extremes, such as the development of extreme events in various regions, the impact of climate change on the frequency of extreme weather, and the influence of extreme conditions on life-history traits. However, the absence of studies in analyzing extreme events in the past interglacial periods is apparent. Knowledge on extreme events during the interglacial period, like the Last Interglacial (LIG) and mid-Pliocene, which are warm or warmer than the contemporary interglacial (Kukla et al.,2002; Raymo et al.,1996), would be valuable to promote our understanding of the human-induced effects on, and trend of, climate extreme events in the predicted warming future.

The LIG is known as the warmest period of the last 200,000 years (e.g., Budyko and Izrael, 1991) and frequently used as a possible analogue for future warming (Langebroek and Nisancioglu, 2013). The concentration of greenhouse gases in the LIG was similar to the Pre-Industrial (PI) period, with carbon dioxide around 275 ppm and methane around 700 ppb, but Earth's orbital eccentricity was more than twice the modern value (Otto-Bliesner et al., 2017). The obliquity was 24.04° and higher than the present value (Otto-Bliesner et al., 2017). Differences in orbital configuration between the two interglacial periods, LIG and PI, lead to the different insolation in the LIG in comparison with PI (Berger, 1978). During boreal summer, the insolation is larger than PI (Otto-Bliesner et al., 2017). Comparing LIG with PI, the higher obliquity results in a small increase in annual insolation anomaly in high latitudes, and a slight insolation decrease in the tropics (Otto-Bliesner et al., 2017). The estimation of temperature increase for the LIG is comparable to the recent estimate of the global temperature increase near the end of the next century by the Intergovernmental Panel on Climate Change (IPCC; Houghton, 1996). Due to warming and heightened boreal thermal seasonality, the LIG is a good analog for future high-latitude climates in the Northern Hemisphere (NH) (Otto-Bliesner et al., 2017).

The mid-Pliocene, about three million years ago (Haywood et al., 2016), is the closest period to present, which was significantly warmer than today (Raymo et al., 1996). The concentration of carbon dioxide was around 400 ppm, and the geography differed from the modern one (Dowsett et al., 2016). There was plausibly a

considerable reduction in Arctic sea ice (Howell et al., 2016; Nooijer et al., 2020), and sea level is estimated to have been 25 m higher (Cronin et al., 1993). High-latitude surface air temperatures and mid-latitude sea surface temperatures may have been 10°C and 3-4°C higher in comparison with today, respectively (Raymo et al., 1996). The PlioMIP2 simulation ensemble shows a raise of 3.7 to 11.6°C in the Arctic (60–90°N) annual mean surface air temperature compared to PI, with a multi-model mean rise of 7.2°C (Stepanek et al., 2020). Finally, at global scale, the average temperatures were increased by almost 2-3°C above the current climate (Jansen et al., 2007). "The mid-Pliocene is attractive for the analysis of future warming because it is geologically recent and therefore similar to today in many aspects." (Robinson et al., 2008). Regarding LIG and mid-Pliocene as analogues for the current and future climates, the LIG is potentially an NH analogue while the mid-Pliocene is conceivably a global analogue (Burke et al., 2018).

This thesis aims to add to our knowledge of climate extremes by addressing these critical questions:

- How do the changes in geography, carbon dioxide concentration, and orbital forcing result in variation of mean temperature and precipitation?
- How do changes in mean values of climate variables lead to alteration in climate extreme indicators?
- Can the LIG and mid-Pliocene be good analogues for the future climate in the case of chosen extreme indices in this thesis?

Toward obtaining the objective of this study, the LIG and mid-Pliocene, which represent to different extents the impact of orbital forcing, geographical changes, and CO_2 on the climate, are chosen as target periods. Furthermore, to emphasize on the role of CO_2 in the ongoing climate warming, a climate state with the current CO_2 concentration of 400 ppm (E400), and one for a more future climate with the CO_2 concentration of 560 ppm (E560), are simulated and analyzed. The analysis of the simulated climates is based on comparison with a simulation of the PI as a reference period.

In this thesis, daily mean outputs of the Max-Planck-Institute Earth System Model (MPI-ESM) and the Community Earth System Models (COSMOS) are employed. The selected climate extreme indicators, the summer day index (SU) and heavy precipitation index (R10), are calculated by means of the Climate Data Operators (CDO).

This master thesis is structured as follows. In chapter 2, the employed models, the experimental design, the CDO, extreme indices, and the necessary statistical methods are described, and the motivation for selecting them is illustrated. Chapter 3 presents climate anomalies for surface temperature, precipitation, and extreme indices. Chapter 4 provides some examples to illustrate how changes in the climate mean influence extreme indices and consequently impact on the severity of climate extremes. Chapter 5 discusses the main question of the thesis. Chapter 6 concludes and summarizes this study.

Chapter 2

Data and Methods

In this chapter, I introduce the models, which are employed for producing daily mean climate outputs, and summarise the experimental setups for the simulations. The necessary statistical methods and CDO are also described. Furthermore, the different categories of extreme indices are defined, and the motivation for the index choice is illustrated.

2.1 MPI-ESM-1-2-LR

The Max-Planck-Institute Earth System Model (MPI-ESM) includes two general circulation models for the atmosphere and the ocean, ECHAM6 and MPIOM, and three subsystem models, for land and vegetation, JSBACH, and for the marine biogeochemistry, HAMOCC5 (Giorgetta et al., 2013; Fig. 2.1).

Fig. 2.1 indicates that ECHAM6, the atmospheric model, is directly linked to the JSBACH land model that represents physical and biogeochemical characteristics of the land cover. The ocean general circulation model, MPIOM, is connected to the HAMOCC model for the marine biogeochemistry. There is also a coupler program named OASIS, which exchanges fluxes for water, energy, momentum, and CO_2 between models and subsystems (Giorgetta et al., 2013).

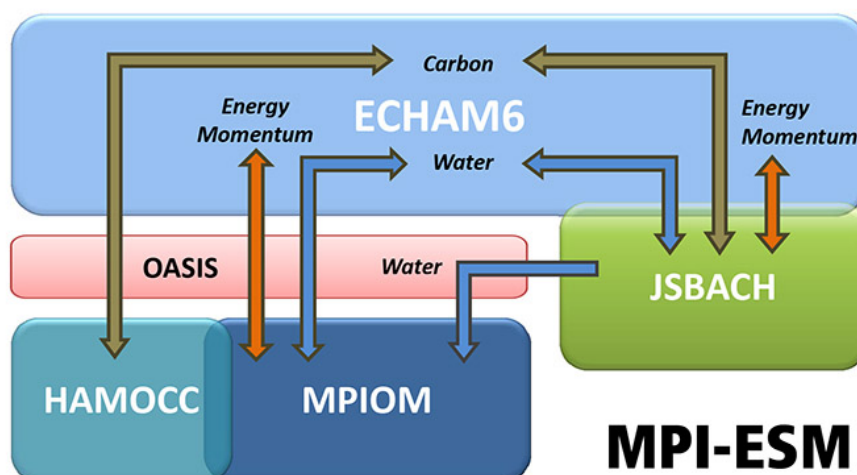


Figure 2.1: Schematic view of MPI-ESM (Giorgetta et al., 2013).

The model system has been produced for a variety of configurations varying in the resolution, orbital forcing and vegetation coverage (Giorgetta et al., 2013). In the MPI-ESM-LR, for the atmosphere a T63 (~ 200 km) global setup with 1.9° horizontal resolution and 47 hybrid sigma pressure levels, and for the ocean a bipolar curved grid with 1.5° resolution (near the equator) and 40 z-levels is chosen. In the MPI-ESM-LR, The poles of the ocean model are moved to Greenland and to the coast of the Weddell Sea by a conformal mapping of the geographical grid. It also uses time steps of 600 s and 4320 s for the atmosphere and the ocean, respectively (Giorgetta et al., 2013).

The low model resolution is an obstacle for a comprehensive assessment of extreme climate indices (Chen and Knutson, 2008), particularly precipitation extreme indices, which could be sensitive to model resolution (Iorio et al., 2004). For instance, global atmosphere-ocean general circulation models (AOGCMs), not resolving spatial scales of less than 300 km, can not present information on the spatial structure of temperature and precipitation in areas of complex geography (Christensen et al., 2007). They also do not provide sufficient information about the atmospheric circulation and processes at high-frequency temporal scales (e.g. precipitation frequency and intensity; Christensen et al., 2007). Hence, the high-resolution climate models are essential for future climate projections, including analyzing extreme climate events (Giorgi et al., 2001). The chosen MPI-ESM model for this thesis has an

adequate resolution to provide the high-resolution daily data sets, which are essential for the study of the climate extreme events (Alexander et al., 2006). In the following, the MPI-ESM refers to MPI-ESM-1-2-LR.

2.2 COSMOS

The Community Earth System Models (COSMOS) consists of an atmospheric-land-vegetation (ECHAM5/JSBACH) model, which is linked with an ocean-sea ice (MPIOM) model by a coupler (OASIS3; Fig 2.2). The COSMOS has been developed at the Max Planck Institute for Meteorology in Hamburg (Germany; Stepanek and Lohmann, 2012).

The atmospheric model (ECHAM5) uses the spatial resolution of T31 ($3.75^\circ \times 3.75^\circ$) with 19 hybrid sigma-pressure levels and a time step of 2400 s (Roeckner et al., 2003). The resolution and number of levels of MPIOM, the ocean model, are GR30 ($3.0^\circ \times 1.8^\circ$) and 40, respectively (Raddatz et al., 2007; Junglauss et al., 2010). The JSBACH, land surface and vegetation model, is a complement for the ECHAM5 model, which uses the same horizontal resolution as the ECHAM5 and receives most of its boundary conditions from the atmosphere model (Raddatz et al., 2007).

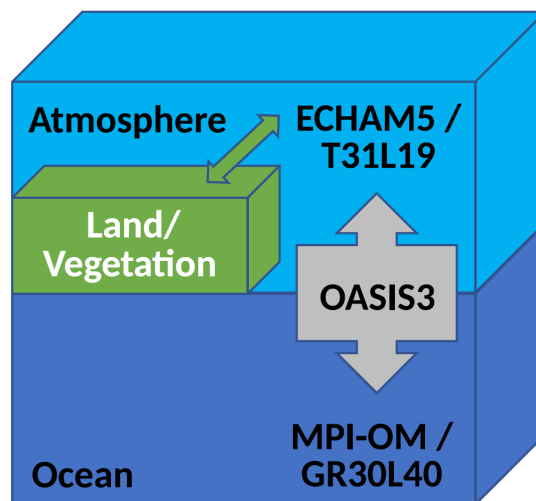


Figure 2.2: Schematic view of COSMOS (Stepanek et al., 2020)

The COSMOS is one of the models contributing to the PlioMIP2 model ensemble (Stepanek et al., 2020). Despite having a low spatial resolution, it has been fre-

quently applied in paleoclimate studies over the Cenozoic, such as by Pfeiffer and Lohmann (2016), Stepanek and Lohmann (2012), Goldner et al. (2014), and Zhu et al. (2020). The noticeable advantage of COSMOS is that it utilises dynamic vegetation and completely resolves climate-vegetation feedbacks. This feature is particularly advantageous in the study of mid-Pliocene in which the vegetation distribution varied significantly from modern (Stepanek et al., 2020). The climate globally controls the spatial distribution of the main vegetation types, and the vegetation cover modifies the climate through the biogeophysical mechanisms and biogeochemical processes (Brovkin et al., 2006). In both local and global scales, the vegetation alteration can trigger many positive and negative feedbacks (Strengers et al., 2010), influencing surface temperature, temperature extremes (Lemordant and Gentine, 2019), and convective precipitation (Strengers et al., 2010). For example, over Europe, a significant part of the amplification of extreme temperatures results from soil moisture feedbacks (Vogel et al., 2017). The dynamic vegetation feature, therefore, is essential to improve climate extremes in simulations.

The MPI-ESM and COSMOS, as two major working models of the last decades of climate research, are employed for this thesis to provide information how climate extremes may look like in common previously used model setup (Sec.2.3). Furthermore, the difference between climate extremes simulated by the two models can be analyzed based on a set of comparable simulations.

2.3 Experimental Design

For every simulation based on a particular geologic period, the model must be adjusted according to the period's characteristics, such as orbital parameters, greenhouse gas concentration, and geography patterns. Regarding the LIG as a good analogue for NH, and mid-Pliocene as a global analogue for the future climate (Burke et al., 2018), in this project, they are selected as the target periods for studying climate extremes of the potential future, and PI is employed as the reference period. Furthermore, concerning the ongoing upward trend of CO_2 concentration, which results in a warmer climate (Houghton, 2001), the models have also been employed to

simulate the conditions with different increased level of CO_2 , 400 ppm (E400) and 560 ppm (E560). There is an important difference between E400 and E560 simulations with the real world. The present climate is not in equilibrium, but E400 and E560 present climates that are in equilibrium. E400 and E560 are analyzed to understand differences between the climate variables (temperature and precipitation) and extreme indicators of purely CO_2 -driven climates (E560 and E400) with LIG and mid-Pliocene, which were formed by orbital forcing and a mixture of drivers (CO_2 and geography changes), respectively.

2.3.1 MPI-ESM-1-2-LR Setup

The MPI-ESM simulations employed here are LIG [Pfeiffer and Lohmann \(2016\)](#), PI, E400, and E560, which have produced 300 years of daily mean outputs for precipitation and temperature. The model setups obey the PMIP4 protocol for simulating LIG and PI with dynamic vegetation ([Otto-Bliesner et al., 2017](#)). For simulation of E560 and E400, the setup is similar to the PI setting, except for CO_2 concentration, which is instantaneously increased to 560 ppm and 400 ppm, respectively. An overview on boundary conditions for the LIG and PI simulation are shown in [Table 2.1](#).

The LIG here refers to 127,000 years before present. This simulation is chosen because it simply tests the response of the climate system to changes in orbital forcing compared to the present ([Otto-Bliesner et al., 2017](#)). The difference in the latitudinal and seasonal distribution of incoming solar radiation (insolation), which results from changes in the Earth's orbit, plays the central role for changes in climate during LIG ([Berger, 1978](#)). Studies on deep-sea sediment cores reveal that temperature peaks in paleoclimate are statistically correlated with the main periodicities in the Earth's orbital parameters, and show that orbital parameters are the main forcing in determining glacials and interglacials ([Hays et al., 1976](#)). Milutin Milankovic described in the 1940's that differences in eccentricity, axial tilt, and precession can significantly change climate patterns by changing the amount of incoming solar radiation (insolation) ([Milankovic et al., 1995](#); [Fig. 2.3](#)).

Table 2.1: Forcings and boundary conditions (Otto-Bliesner et al., 2017) of MPI-ESM simulations employed in this thesis

Boundary Conditions	Last Interglacial (LIG)	Preindustrial (PI)
Orbital Parameters		
Eccentricity	0.039378	0.016764
Obliquity (degrees)	24.040	23.459
Perihelion-180°	275.41	100.33
Vernal equinox	Fixed to noon on March 21	Fixed to noon on March 21
Greenhouse Gases		
Carbon dioxide (ppm)	275	284.3
Methane (ppb)	685	808.2
Nitrous oxide (ppb)	255	273
Other Parameters		
Solar constant ($W.m^{-2}$)	Same as PI	1360.747
Geography	Same as PI	Modern
Ice sheets	Same as PI	Modern

In the LIG, the axial tilt was greater (24.04° , rather than 23.46° as today; Table 2.1), which caused stronger insolation in the boreal summer and weaker insolation in the boreal winter. Furthermore, the Earth moves through perihelion, the point where Earth is closest to the Sun, during boreal summer at the LIG, while at present it reaches perihelion during NH winter (Harrison et al., 1995). Thus, the different orbital configurations for the LIG and PI lead to different seasonal and latitudinal distribution of incoming solar radiation at top of the atmosphere. The solar constant prescribed for the LIG simulation is the same as in the PI (Eyring et al., 2016). Since GHG is a significant factor influencing the climate system, simulations have to take GHG into account to respond correctly. Ice core records provide measurements of the well-mixed GHGs: CO_2 , CH_4 , and N_2O . Because of potential in-situ CO_2 production in the Greenland ice sheet, CO_2 concentrations can only be derived from Antarctic ice (Tschumi and Stauffer, 2000). Besides, there are not any reliable CH_4 and N_2O records from Greenland in the LIG due to melting of the ice layers, as Greenland temperatures were significantly warmer at that time compared to the mean of the past millennium (Otto-Bliesner et al., 2017). During the LIG the

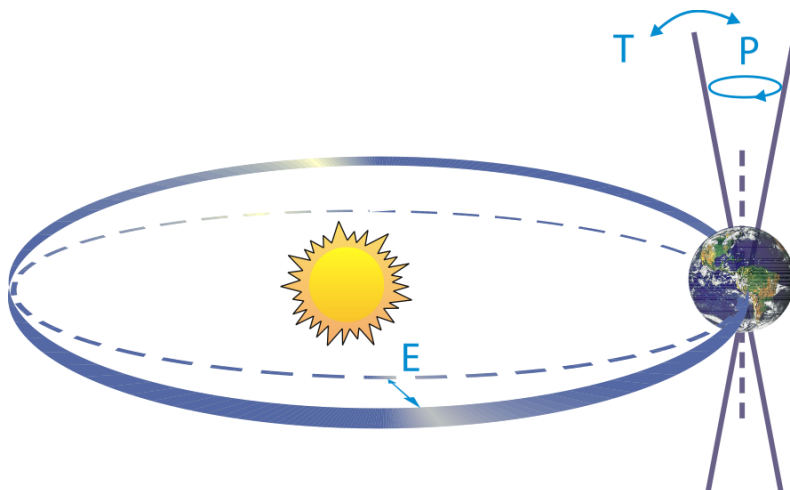


Figure 2.3: Schematic of the Earth's orbital variations (Milankovitch cycles). "T" is used for changes in the Earth's axis tilt, "E" for changes in the eccentricity of the orbit, and "P" for precession (Pachauri and Reisinger, 2008).

concentrations of atmospheric CO_2 and CH_4 had risen from their respective levels during the previous glacial periods to values comparable to PI levels (Otto-Bliesner et al., 2017).

DeConto and Pollard (2016) suggest that the West Antarctic ice sheet is a significant contributor to LIG global mean sea-level rise. The marine-based portions of the East Antarctic ice sheet also contribute to sea-level rising (DeConto and Pollard, 2016). These contributions can explain the global mean sea level rise of 6 m during the LIG (Dutton et al., 2015), but due to the complexity in fulfilling ice-to-ocean changes, the palaeogeography and ice sheet of the LIG simulation is designed as same as in the PI simulation (Table 2.1; Otto-Bliesner et al., 2017).

2.3.2 COSMOS Setup

The COSMOS has been used to simulate the mid-Pliocene, PI, LIG, E400, and E560. The simulations have provided 300 years of daily mean output for temperature and precipitation. Simulations for the future (E560 and E400), mid-Pliocene, and PI are based on model configurations which are precisely presented by Stepanek et al. (2020). The setup of the COSMOS simulation for the LIG is described by Pfeiffer and Lohmann (2016). Table 2.2 summarizes the boundary conditions of COSMOS simulations used in this thesis. In the E400 and E560 simulations, the

settings are similar to PI except for CO_2 concentration, which increases to 400 ppm and 560 ppm, respectively (Stepanek et al., 2020).

Table 2.2: Forcings and boundary conditions of COSMOS simulations employed in this thesis (Pfeiffer and Lohmann, 2016; Stepanek et al., 2020)

Boundary Conditions	Last Interglacial	Preindustrial	mid-Pliocene
Orbital Parameters			
Eccentricity	0.0382	0.016724	0.016724
Obliquity (degrees)	24.24	23.446	23.446
Perihelion-180°	49.1	282.04	282.04
Greenhouse Gases			
Carbon dioxide (ppm)	280	280	400
Methane (ppb)	760	808	808
Nitrous oxide (ppb)	270	273	273
Other Parameters			
Solar constant ($W.m^{-2}$)	1367	1367	1367
Geography	same as PI	modern	PRISM4
Ice sheets	same as PI	modern	PRISM4

The COSMOS simulations for mid-Pliocene and PI generally follow the PlioMIP2 protocol (Stepanek et al., 2020). The different simulated climates for mid-Pliocene and PI result from variations in CO_2 concentration and geography between these two time periods, which are based on the PRISM4 mid-Pliocene reconstruction by Dowsett et al. (2016). According to the PlioMIP2 protocol (Haywood et al., 2016), the volume mixing ratio of 400 ppm is selected, which is compatible with the range of paleo-reconstructions of CO_2 during the Pliocene, between 360 ppm (Kürschner et al., 1996) and 425 ppm (Raymo et al., 1996). The concentrations of CH_4 and N_2O for the mid-Pliocene simulation, are the same as those of the PI, which are suggested by Otto-Bliesner et al. (2017).

The change in the land-sea mask, which is modified from modern conditions, is the most noticeable difference in PlioMIP2 compared to the PlioMIP1 model setup (Stepanek and Lohmann, 2012; Stepanek et al., 2020). The ocean bathymetry, the earth surface geopotential, and topography are computed as an anomaly from PRISM4 modern conditions by equations offered by Haywood et al. (2016).

2.4 The Climate Data Operators (CDO)

The Climate Data Operator (CDO) software is a group of various operators which can process climate and forecast model data. The operators perform simple statistical and mathematical functions, data selection and subsampling, and spatial interpolation. CDO was developed to have the same set of processing functions for GRIB (General Regularly-distributed Information in Binary form) and NetCDF (Network Common Data Form) datasets in one package (Schulzweida et al., 2006). The main CDO features, which are employed for the conduct of this thesis, are:

- straightforward UNIX command-line interface. A dataset can be processed by serial execution of several consecutive operators, without storing the interim results in files, which is of paramount importance to process the large volume of daily model output in a practical manner.
- fast processing of large datasets
- dedicated operators for computing the extreme indices
- support of the ECHAM6 T63 Gaussian Grid and ECHAM5 T31 Gaussian Grid including automatic area weighting in averaging function.

2.5 Climate Extreme Indices

Climate extreme indices are defined to answer the questions about the trend of climate extremes events, having impacts on society and natural system (Alexander et al., 2006; Zhang et al., 2011). In order to analyze global changes in climate extremes, it is essential to develop a set of climate extreme indices that are statistically robust and cover different types of climates (Zhang et al., 2011). Internationally accepted indices obtained from daily mean temperature and precipitation allow researchers to compare climate extremes systematically across different regions and also have the advantage of overcoming most of the constraints on the dissemination of daily data that are applied in many countries (Zhang et al., 2011). Regarding the ability of the climate extreme indices in representing climate extremes in different

climates and the simulated daily data sets, two extreme climate indices are chosen and analyzed to show the changes in climate extremes in the simulated climates used in this thesis.

Before introducing different types of climate extreme indices, it is worth showing how the changes in the average of climate variables statistically result in variations of climate extremes. Figure 2.4 displays schematic illustrations of the probability distributions of daily temperature, which tend to be approximately Gaussian, and daily precipitation, the latter having a skewed distribution (Zwiers et al., 2013). However, soil freezing, feedback processes, or energy balance constraints can alter the shape of temperature probability density functions (Fischer and Schär, 2009; Zazulie et al., 2010; Mueller and Seneviratne, 2012). In the case of temperature, variations in the frequencies of extremes are greatly affected by changes in the mean; a moderately small shift of the distribution towards higher temperature would substantially increase warm extremes and decrease cold extremes (Zwiers et al., 2013). Furthermore, the rate of extremes can also be affected by changes in the shape of the tails of the temperature distribution, which could become broader or narrower, or could become somewhat skewed rather than being symmetric as depicted. In a skewed distribution of precipitation, a change in the mean of the distribution generally affects its variability or spread. Consequently, an increase in mean precipitation would also likely imply an increase in massive precipitation extremes, and vice-versa. Furthermore, the shape of the right-hand tail could also change, affecting extremes (Zwiers et al., 2013).

Expert Team on Climate Change Detection, Monitoring and Indices (ETCCDMI) recommend 27 indices, of which 16 are related to temperature, and 11 are related to precipitation. These indices are derived from daily maximum and minimum temperature and daily rainfall (Alexander et al., 2006). These indices were based on the European Climate Assessment (ECA) indices and chosen to sample a wide variety of climates. They included indicators such as the total number of frost days, summer days, and the maximum number of consecutive dry days in a year (Frich et al., 2002). Main differences in various indices of extremes are how the distribution was defined, and where the index threshold is placed (Zwiers et al.,

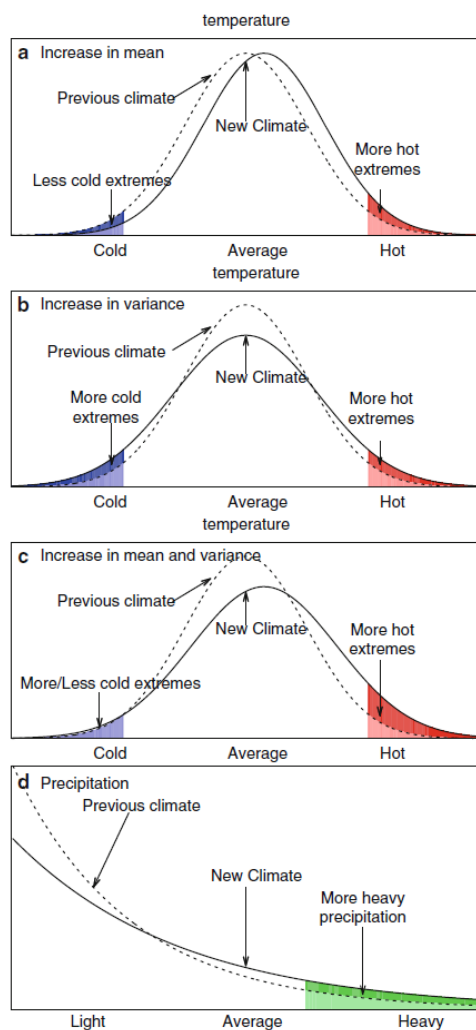


Figure 2.4: Schematic of the probability distributions of daily temperature and precipitation. Extremes are expressed by shaded areas (Zwiers et al., 2013).

2013). Generally, the extreme indices can be categorised into five classes:

- absolute indices, showing minimum or maximum values within a season or year; for instance, the temperature of the hottest or the coldest day of the year, or the annual maximum of one day or five day precipitation rates
- threshold indices, computing the number of days when temperature or precipitation values exceed the determined threshold; for instance, summer days or heavy precipitation index

- duration indices, describing the length of wet and dry spells, or of warm and cold spells
- percentile-based indices, which describe the exceedance rates above or below a threshold, defined as a percentile which is derived from a reference period
- other indices, which do not fall into any of the above categories, including indices of annual precipitation total (PRCPTOT), diurnal temperature range (DTR), simple daily intensity index (SDII), extreme temperature range (ETR) and annual contribution from very wet days (R95pT; [Alexander et al., 2006](#)).

In this project, the following indices have been selected and are computed by means of CDO:

- The summer days index (SU) indicates the number of days when daily maximum temperature (TX) is above 25°C . Let TX_{ij} be daily maximum temperature on day i in year j . The value of SU is defined via a count of the number of days where:

$$TX_{ij} > 25^{\circ}\text{C} \quad (2.1)$$

The summer days index is one of the indices which expresses the intensity of warm seasons and is often useful for climate impact studies ([Klein Tank and Können, 2003](#)).

- The heavy precipitation index (R10) shows the number of days when daily precipitation is above 10 mm. Let RR_{ij} be the daily precipitation amount on day i in period j . The value of R10 count the number of days where:

$$RR_{ij} \geq 10\text{mm} \quad (2.2)$$

The R10 is one of the indices characterizing the wet part of the year, and also highly correlated with total annual and seasonal precipitation in most climates ([Frich et al., 2002](#)).

Both selected indices are threshold-based, characterizing aspects of the far tail of the distribution. This kind of index is more relevant to society and natural systems than the indices that describe aspects of the distribution that occur frequently (Zwiers et al., 2013). The select of threshold-based indices make the anomaly calculations of indices simple because they do not require a reference period. Therefore, the climate extreme indices for all simulations are calculated, and then, their anomaly with respect to the PI can be plotted. Furthermore, the heavy precipitation index and the summer days index have been frequently used in published papers such as Frich et al. (2002), Alexander et al. (2006), Zhang et al. (2005), de los Milagros Skansi et al. (2013), and Sillmann et al. (2013). Due to the above reasons, the heavy precipitation index and summer days index have been chosen to be analyzed for the different simulations.

2.6 T-Test Analysis for Comparing Climate Anomalies

The t-test is one of the more basic statistical procedures for hypothesis testing. There are several kinds of t-tests. However, the most common is the two-sample t-test, also known as the Student's t-test or the independent samples t-test, which is used for analysing the mean value data sets to indicate insignificant anomalies. The independent samples t-test examines whether the means of two sets of data differ significantly; the data belong to two different sets of subjects under different conditions (O'Mahony, 1986).

$$t = \frac{\text{difference between means}}{\text{standard error of difference}} = \frac{\bar{X} - \bar{Y}}{s_{\bar{\Delta}} = \sqrt{\frac{s_1^2}{n_1} + \frac{s_2^2}{n_2}}} \quad (2.3)$$

In Eq. 2.3, \bar{X} and \bar{Y} are the means for the two independent samples, and s_i^2 is the unbiased estimator of the variance of each of the two samples with n_i being the number of samples in group i. If $\bar{X} - \bar{Y}$ is large compared to the standard error

of the difference, t will be large. The standard error term can be identified as a measure of the potential random variation, or experimental error, in the experiment. Therefore, if differences between the two samples are substantial compared to experimental deviation or noise, the two samples are significantly different (t is large; O'Mahony, 1986). In this thesis, the two-sample t -test is applied to identify insignificant difference in the temperature and precipitation anomalies of the different simulated climates minus PI.

2.7 Kolmogorov–Smirnov Test

The Kolmogorov-Smirnov test examines if two datasets differ significantly. The underlying assumption for this test is that the continuous distributions of the samples are unknown. The test calculates the maximum absolute deviation between the two distribution functions (Magel and Wibowo, 1997). The two-sample Kolmogorov-Smirnov is one of the most useful and general non-parametric methods for comparing two samples because it uses all data points in the samples, and it is independent of distribution and the direction of the ordering of the data (Lopes et al., 2007). Consider two independent random variables, X and Y , with distributions $F(x)$ and $G(x)$. The null-hypothesis

$$F(x) = G(x), \text{ for all } x \quad (2.4)$$

versus

$$F(x) \neq G(x), \text{ for some } x \quad (2.5)$$

can be tested by the Kolmogorov-Smirnov statistics. The Kolmogorov–Smirnov statistic is

$$D_{n,m} = SUP | F_n(x) - G_m(x) |, \quad (2.6)$$

where F_n and G_m are empirical distributions of two samples, n and m are the respective sizes of the samples, and SUP is a supremum function. The null-hypothesis at the level of α will be rejected if:

$$D_{n,m} > C(\alpha) \sqrt{\frac{n+m}{n.m}} \quad (2.7)$$

The value of $C(\alpha)$ is given in table 2.3 by [Young \(1977\)](#) and produced here for the most common values of α .

Table 2.3: Value of $C(\alpha)$ for different levels of α reproduced from [Young \(1977\)](#).

α	$C(\alpha)$
0.1	1.22
0.05	1.36
0.01	1.63
0.005	1.73
0.001	1.95

The Kolmogorov-Smirnov test is a powerful test for large data sets ([Wilcox, 1997](#)). It is also used for comparing the probability density functions (PDF) of extreme indices in many published papers such as [Alexander et al. \(2006\)](#) and [Russo and Sterl \(2011\)](#). In this thesis, the two-sample Kolmogorov-Smirnov test, with a null hypothesis that two cumulative distribution functions computed for two simulations are identical, is used to show whether the probability distributions of a particular index from different climate simulations are significantly different or not.

Chapter 3

Simulated Mean Climate and Extremes

In the following, the surface temperature and precipitation as simulated by MPI-ESM and COSMOS, and extremes indices calculated by means of CDO, are presented and interpreted for their differences in the boreal summer, winter, and annual mean. Summer and winter in the northern hemisphere (NH) are defined as June-July-August (JJA) and December-January-February (DJF), respectively. The surface temperature, in this thesis, is 2 meter temperature above the surface. Moreover, the precipitation imply sum of the convective and large-scale precipitation.

3.1 MPI-ESM

3.1.1 Surface Temperature

The annual mean surface temperature during the LIG, shows large scale warming, increasing toward high latitudes. At mid-latitudes, the anomaly is 1°C , and it increases to 3°C in polar regions. A strong cooling of 5°C is observed in the Sahel region and Indian subcontinent in both summer and winter. A warmer summer in the NH (Fig. 3.1a), notably between 30° and 70°N , is seen (up to around 8°C higher). During, boreal winter, the regions from the Barents Sea and the Kara Sea to the Greenland, Norwegian, and Iceland Seas face warming (from 1° to 5°C),

while mid-latitudes regions encounter pronounced cooling in the NH. In general, it is evident that warming and cooling are more powerful across landmasses than over oceans, and the land-sea contrast is more robust for both seasons. The annual temperature anomaly for PI and LIG differs from -5°C to around 3°C .

In simulation E400 (Fig. 3.1b), the annual temperature anomaly shows a global rise by 2°C and 5°C . However, in the Barents Sea and the Kara Sea, an increase up to 9°C is observed. In the tropics and subtropics, the land anomaly is greater than the ocean anomaly. The strong positive temperature anomaly is clearly seen in high latitudes and Arctic during the boreal summer. Moreover, the temperature anomaly pattern in E560 is the same as in E400, but warming is more intensive than for E400 (Fig. 3.1c). The global average temperature in LIG, E400, E560, and PI is shown in Table 3.1. E560 globally represent the warmest climate, and the PI is warmer than LIG by just 0.5°C . It is clearly evident that increase of CO_2 concentration results in a global warming in both boreal winter and summer (Fig. 3.1).

3.1.2 Precipitation

Fig. 3.2a shows that summer monsoons, covering the Sahel zone and South Asia are stronger during the LIG than for PI. Such monsoons are caused by the land-sea pressure and temperature contrast, which strengthens the moist onshore inflow to the land. Besides, precipitation associated with the Inter-tropical Convergence Zone (ITCZ) in the LIG is higher as compared to the PI. Furthermore, the boreal winter monsoon is weaker over South Africa, South America, and Australia, and heavier over the western Indian Ocean and the western Pacific Ocean (Fig. 3.2a). Except for the regions influenced by ITCZ, the many land regions such as North America, South America, the centre of Asia, and the south of Africa experience drier conditions during the LIG. However, the global average precipitation difference between LIG and PI is just 10 mm/year (Table 3.1).

Fig. 3.2b indicates many regions in which the precipitation difference is insignificant between the E400 and PI simulations. In most regions, particularly land regions, the precipitation in E400 is slightly higher than that of PI. However, in the tropics and

subtropics, the negative anomalies are observed. The global average of precipitation in E400 is around 1063 mm/year, which suggests that there are small differences in global average precipitation between E400, PI (1035 mm/year), and E560 (1089 mm/year; Table 3.1). Nevertheless, the local differences in precipitation in many regions are pronounced. For instance, the orbitally driven LIG shows strong impact of precipitation change in the Sahel zone while purely CO_2 driven simulation E400 and E560 only provide a modest change in that region. The precipitation anomaly pattern in E560 (Fig. 3.2c) is similar to E400; although, the anomalies in E560 are stronger than E400 anomalies.

3.1.3 Climate Extreme Indices

In all simulations, there is a strong relation between the boreal summer temperature pattern (Fig. 3.1) and summer days index (Fig. 3.3). The anomaly in summer days index is often identified in all regions except for the polar regions because the daily maximum temperature in polar regions does not exceed 25°C in the simulations. During the LIG, due to the cooling effect of stronger monsoons, a noticeable negative anomaly is observed in the Sahel zone and India; moreover, the amplitude of summer days index considerably increases in the centre of North America and the south of South America (Fig. 3.3a). Comparing PI with E560 and E400, the patterns of summer days index represent more extreme warm days over all continents, particularly in South America and the south of Africa (Fig. 3.3b; Fig. 3.3c). Table 3.1 presents that the increase in the global average of temperature is highly associated with the rise in the average number of summer days index, which is computed by averaging over all land areas. The heavy precipitation index (Fig. 3.4) almost tracks the annual precipitation patterns (Fig. 3.2). During the LIG, due to stronger monsoons compared to PI, the extreme rain events increase in the Sahel zone and the south of Asia. The number of heavy precipitation days also rises over the Central America. The strong anomalies are often located between the Equator and 40° latitudes with a considerable reduction in Southeast Asia (Fig. 3.4a). In E400, in comparison to PI, the heavy rainfall extremes do not differ in most regions (Fig. 3.4b). However, the variations in heavy precipitation index in E560 are more

pronounced than in E400, which suggest that increase of CO_2 concentration can significantly alter the trend of the extreme precipitation events (Fig. 3.4c). In contrast to the LIG, the extreme rain events slightly rise over the NH between the latitudes 40° and 80° in E560. For example, there are modest increases in heavy precipitation index over the north and north-west of Europe, the eastern coast of Greenland, Gulf of Alaska; and over the oceans in the southern hemisphere (SH) (40° and 60° latitudes), slight increases in rain extremes are also seen (Fig. 3.4c). Furthermore, in E560, a pronounced positive anomaly is observed in the Pacific ocean over the Equator. In general, the minor changes in the global average precipitation (between 10 to 56 mm/year) do not result in pronounced variations in the global average of the heavy precipitation index (Table 3.1). However, there are many critical local changes in extreme rain events linked to changes in orbital forcing (in the LIG) or CO_2 forcing (E560). For example, the orbital forcing is the dominant factor for the occurrence of heavy precipitation events over Central America, the centre of Africa, and India (Fig. 3.4a) while the CO_2 plays the central role in the increase of the heavy rain extremes in high latitudes particularly in the NH (Fig. 3.4c).

Table 3.1: Global annual average of temperature, precipitation, SU, and R10 for MPI-ESM simulations.

Simulation	Average Temperature ($^\circ C$) \approx	Average SU (day/year) \approx	Average Precipitation (mm/year) \approx	Average R10 (day/year) \approx
LIG	13.41	109	1045	33
E400	15.01	137	1063	34
E560	16.51	154	1089	35
PI	13.53	116	1035	32

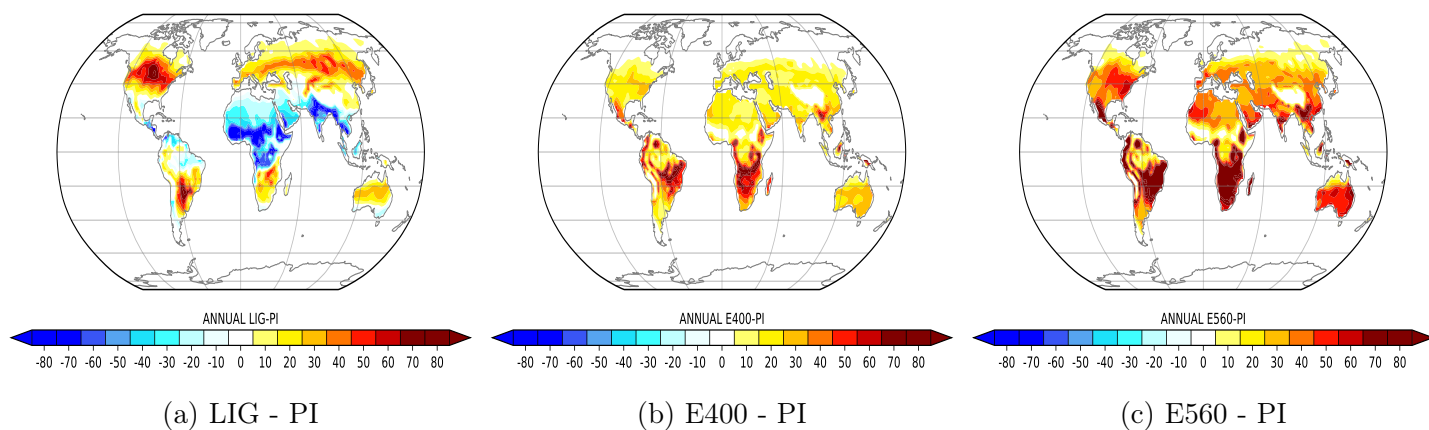


Figure 3.3: Summer days index anomaly for MPI-ESM simulations, LIG minus PI (a), E400 minus PI (b), and E560 minus PI (c). The unit is days/year.

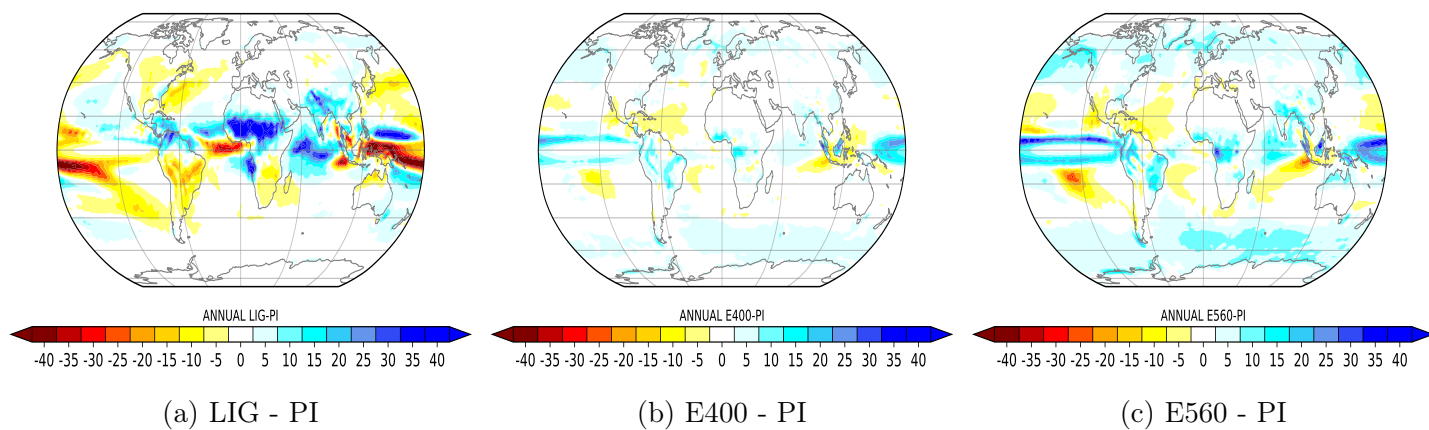


Figure 3.4: Heavy precipitation index anomaly for MPI-ESM simulations, LIG minus PI (a), E400 minus PI (b), and E560 minus PI (c). The unit is days/year.

3.2 COSMOS

3.2.1 Surface Temperature

In general, the warming is frequently observed in all regions in the mid-Pliocene simulation (Fig. 3.5b). Most significant anomalies, exceeding 14°C , are visible in polar regions such as Greenland, west and east of Antarctica. This warming in polar regions suggests a pronounced reduction or the absence of ice sheets in the mid-Pliocene, which can trigger a positive feedback resulting in more warming. There are only a few regions that show no changes or very slight negative anomalies. These regions are mainly over or near the lands such as the middle of Antarctica, east of Asia, south-east of Asia, and the Sahel. In the NH, the warming of the high latitudes in the winter is stronger than summer, which means that the seasonality reduces in comparison to PI (Fig. 3.5b). The significant differences in the simulated mid-Pliocene climate are caused by modifying geography and carbon dioxide concentration compared to the PI simulation.

Fig. 3.5a shows that the seasonality in the LIG is more robust than that of PI, as the temperature anomalies in the boreal winter and summer are significantly different. This strong seasonality results from different orbital configurations defining the LIG climate. Moreover, the impact of the ITCZ on the Sahel zone and India is clear, which causes negative anomalies in these regions during the LIG.

Comparing the CO_2 driven simulations, E400 and E560, global warming is seen with respect to PI; however, the anomalies in E560 indicate more increases, particularly in polar regions and high latitudes (Fig. 3.6). Both mid-Pliocene and E560 simulations illustrate noticeable warming in polar regions, but in the mid-Pliocene, the positive anomalies are more powerful. In addition, some negative anomalies are recognisable in the mid-Pliocene, which are not seen in the E560 (Fig. 3.6b, Fig. 3.5b). These observations propose that the combination of geography changes and 400 ppm CO_2 concentration (drivers of mid-Pliocene climate) are more effective in polar regions while the CO_2 driven climate (E560) represents more a global warming.

3.2.2 Precipitation

In contrast to the surface temperature anomalies, the precipitation anomalies follow diverse spatial patterns during the mid-Pliocene (Fig. 3.7b). The most negative anomalies are detected in the tropic and subtropic regions in the SH. However, the precipitation significantly decreases in some regions in the NH such as East Asia, south-east of Asia, the centre of the North Atlantic, and east of North America. In general, the anomalies slightly decrease from around 40° polewards (Fig. 3.7b). The rainfall increases over the Arctic and Antarctica except for the west coast of Antarctica. From the boreal summer to winter, during mid-Pliocene, a noticeable growth in precipitation amount is observed over North and Northwestern Europe, Norwegian Sea, and the Greenland Sea while the precipitation reduces in South Europe and over the Mediterranean Sea.

Fig. 3.7a and Fig. 3.7b illustrate that the anomalies during the mid-Pliocene are more robust than for the LIG except for the Sahel zone and India in the boreal summer because of more powerful monsoons in the orbitally driven LIG. The increased northern hemisphere solar radiation during the LIG produced a larger land-ocean pressure gradient, stronger winds, and greater precipitation over the southern Asia and North Africa (Prell and Kutzbach, 1987).

The precipitation pattern for CO_2 driven simulations, E400 and E560, are similar, but the anomalies in E560 are more pronounced compared to E400 (Fig. 3.8). This pattern suggests that the differences in precipitation become stronger via an increase of CO_2 concentration. In both simulations, monsoons over the Sahel and India weaken, and even a noticeable reduction in precipitation is observed over India for E560 (Fig. 3.8b). Furthermore, the negative anomalies are mostly restricted from the equator to 60° latitudes during E400 and E560 (Fig. 3.8).

3.2.3 Climate Extreme Indices

During the LIG, the extreme summer days significantly decrease in the regions affected by the ITCZ, such as Sahel, India, and south-east of Asia (Fig. 3.9a). This pattern means that the ITCZ plays a key role in the cooling of those regions during

summer. Fig. 3.9 demonstrates that the global distribution of the summer days index in mid-Pliocene, E400, and E560 follows the same pattern, which implies that a rise of CO_2 concentrations results in more extreme summer days in comparison with PI. However, the anomalies in E560 are more pronounced in comparison with mid-Pliocene and E400. Comparing Fig. 3.9b and Fig. 3.9c, it is evident that the impact of combination of geography and CO_2 changes is more influential than that of the increase in CO_2 concentration on the warm summer days. The most intensive anomalies are observed in South America and the south of Africa, in tropics regions. In contrast, there are no anomalies in the polar regions. Table 3.2 shows that on average, the E560 has the maximum of summer days, which is associated with the highest average temperature. Therefore, the most robust warming leads to the sharpest increase in summer heat extremes. In general, the relation between temperature increase and summer days index nonlinear. For example, a modest change in temperature in E400 compared to E560 (Fig. 3.6), can lead to a huge increase in summer days (Fig. 3.9c, Fig. 3.9d).

The heavy precipitation patterns in all simulations (Fig. 3.10) almost obey the patterns of precipitation (Fig. 3.7, Fig. 3.8). In the LIG, the heavy precipitation events slightly increase over the Sahel, south-west of Asia and India as a result of powerful monsoons; however, moderate reductions are seen in the east and south-east of Asia, south of Africa and some regions in North and South America. Moreover, in high latitudes, the heavy precipitation index does not change during the LIG compared to PI (Fig. 3.10a).

In the mid-Pliocene, Malaysia, the Arabian Sea, and the West Pacific near the Equator experience noticeable increase in heavy rain days. A slight to moderate growth is also observed over Europe, the north of the Atlantic, Alaska Bay, the Sahel, and India. Nevertheless, the heavy precipitation events decline in South America, the west of North America, the south of Africa, east of Asia, and mainly south-east of Asia over the Indian Ocean in where the negative anomaly is pronounced (Fig. 3.10b).

In the E560 simulation, the heavy precipitation index follows the same pattern as in E400, but the differences are amplified in the E560 simulation (Fig. 3.10c,

Fig. 3.10d). In E560, the regions, showing a reduction in extreme rainfall events compared to PI, are located between the Equator and 60° latitudes. However, in the Pacific over the Equator and the Arabian sea, the heavy precipitation days considerably increase in E560. Comparing E560 with the LIG (Fig. 3.10), there are more extreme rainfalls from 60° to 80° latitudes in E560. These results propose that CO_2 concentration change is more effective than the orbital change in heavy precipitation events over the high latitudes.

Table 3.2 indicates that in the global average, the annual precipitation and heavy precipitation index do not noticeably change in the simulations. Nevertheless, the strong regional anomalies in heavy rainfall extremes are evident. In general, the heavy precipitation anomalies in E560 and the mid-Pliocene are more pronounced compared to LIG, showing the importance of both geographical changes and CO_2 forcing for rain extremes.

Table 3.2: Global annual average of temperature, precipitation, SU, and R10 in COSMOS simulations.

Simulation	Average Temperature (°C) \approx	Average SU (day/year) \approx	Average Precipitation (mm/year) \approx	Average R10 (day/year) \approx
Mid-Pliocene	16.89	154	1053	35
LIG	13.81	116	1004	33
E400	15.66	144	1037	35
E560	18.21	170	1088	37
PI	13.51	116	995	33

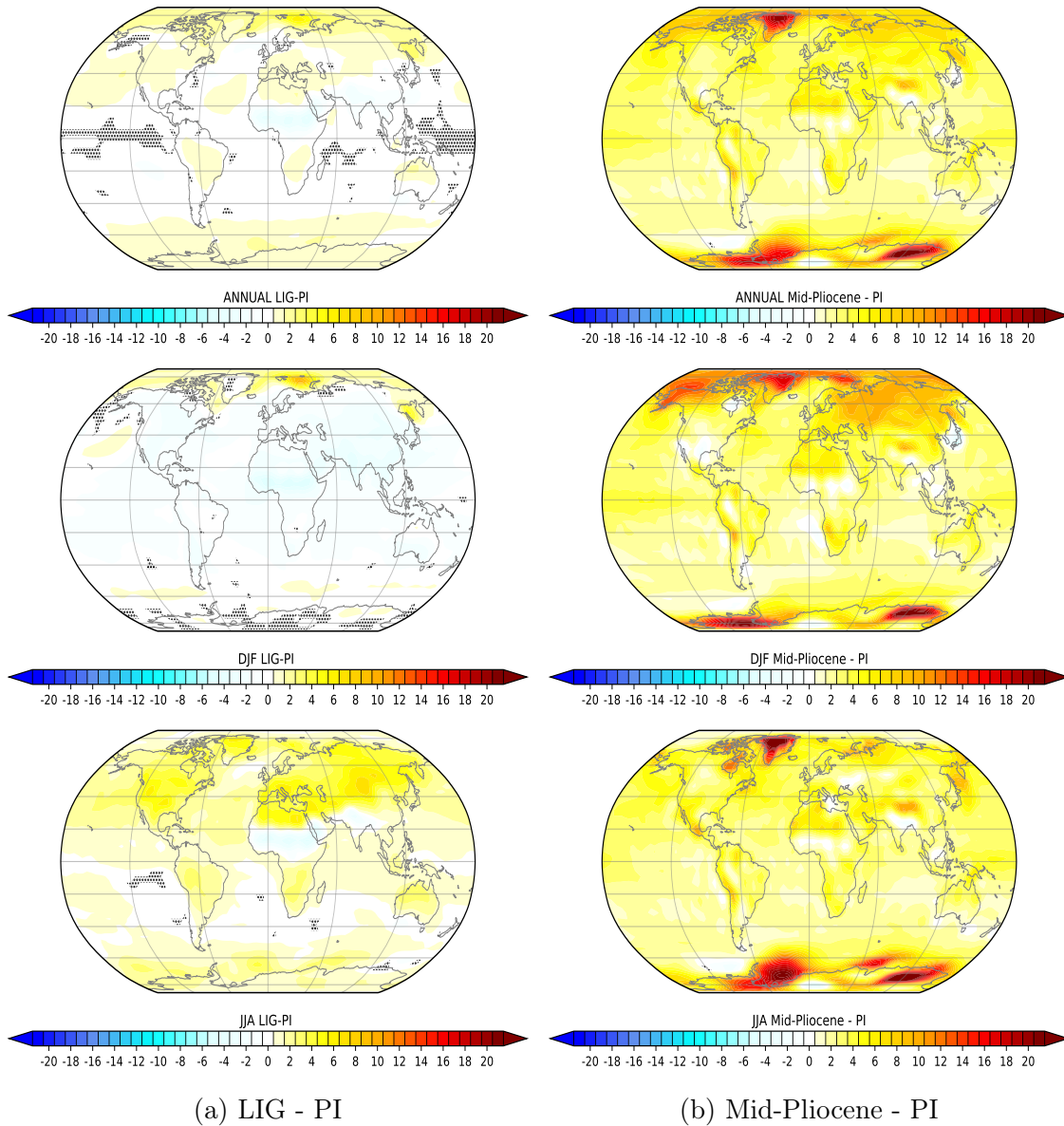


Figure 3.5: Surface temperature anomaly for COSMOS simulations, LIG minus PI (a) and mid-Pliocene minus PI (b). The unit is $^{\circ}\text{C}$. The hatched areas indicate regions where the anomaly is insignificant based on a t-test with 95% confidence interval. The anomaly in (b) is almost everywhere significant.

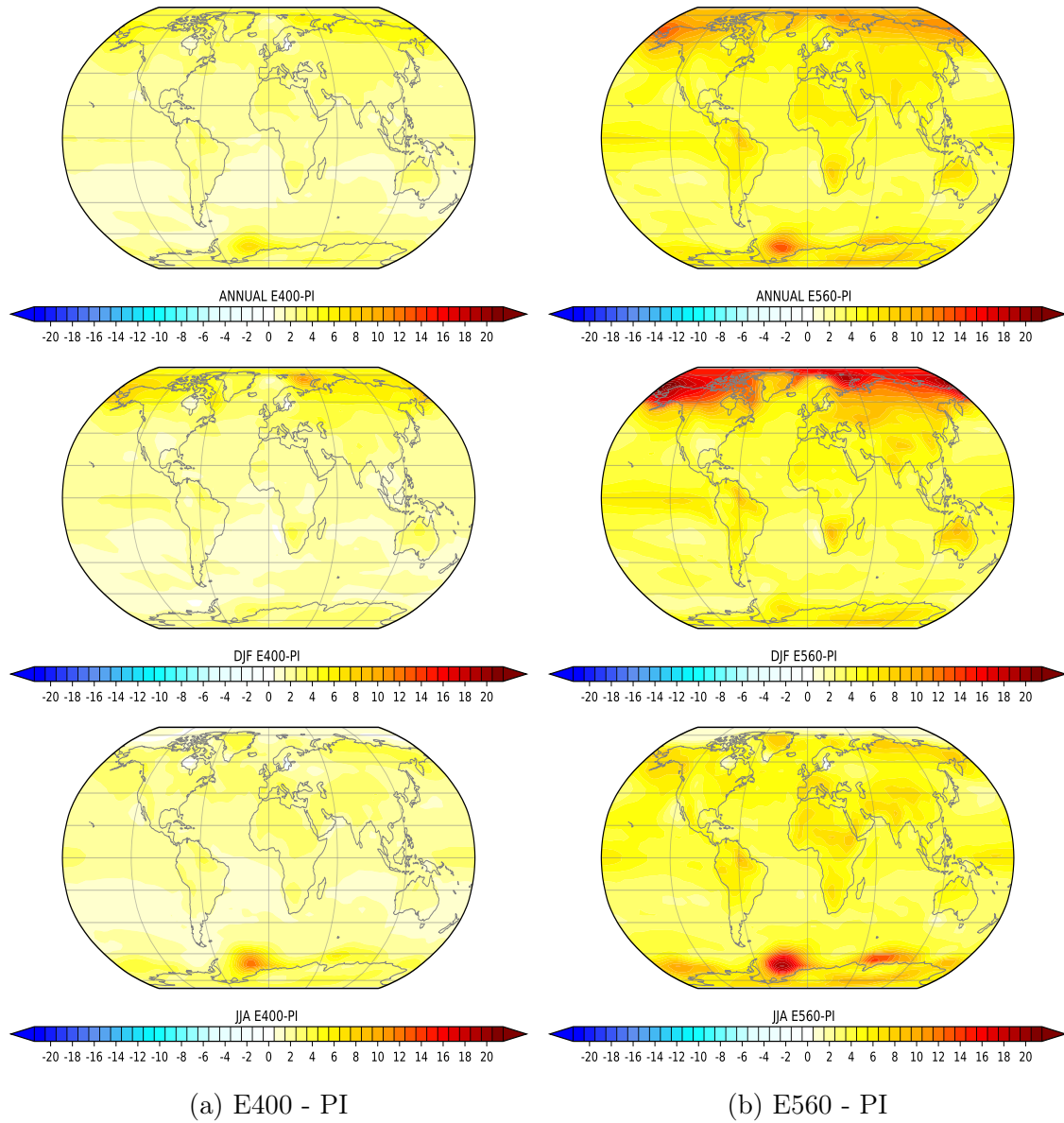


Figure 3.6: Surface temperature anomaly for COSMOS simulations, E400 minus PI (a) and E560 minus PI (b). The unit is °C. The anomalies are almost everywhere significant based on a t-test with 95% confidence interval.

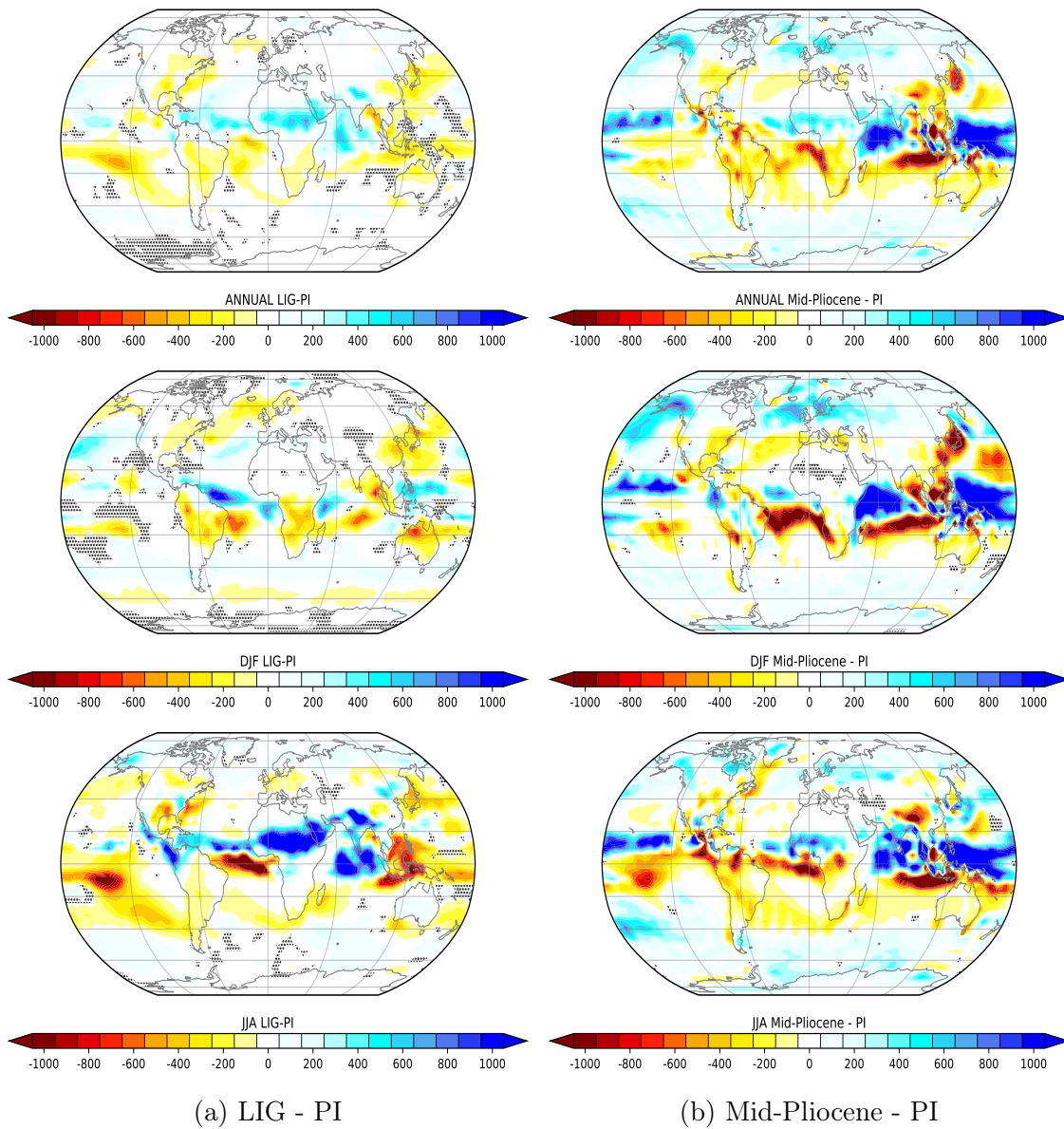


Figure 3.7: Precipitation anomaly for COSMOS simulations, LIG minus PI (a) and mid-Pliocene minus PI (b). The unit is mm/year. The hatched areas indicate regions where the anomaly is insignificant based on a t-test with 95% confidence interval.

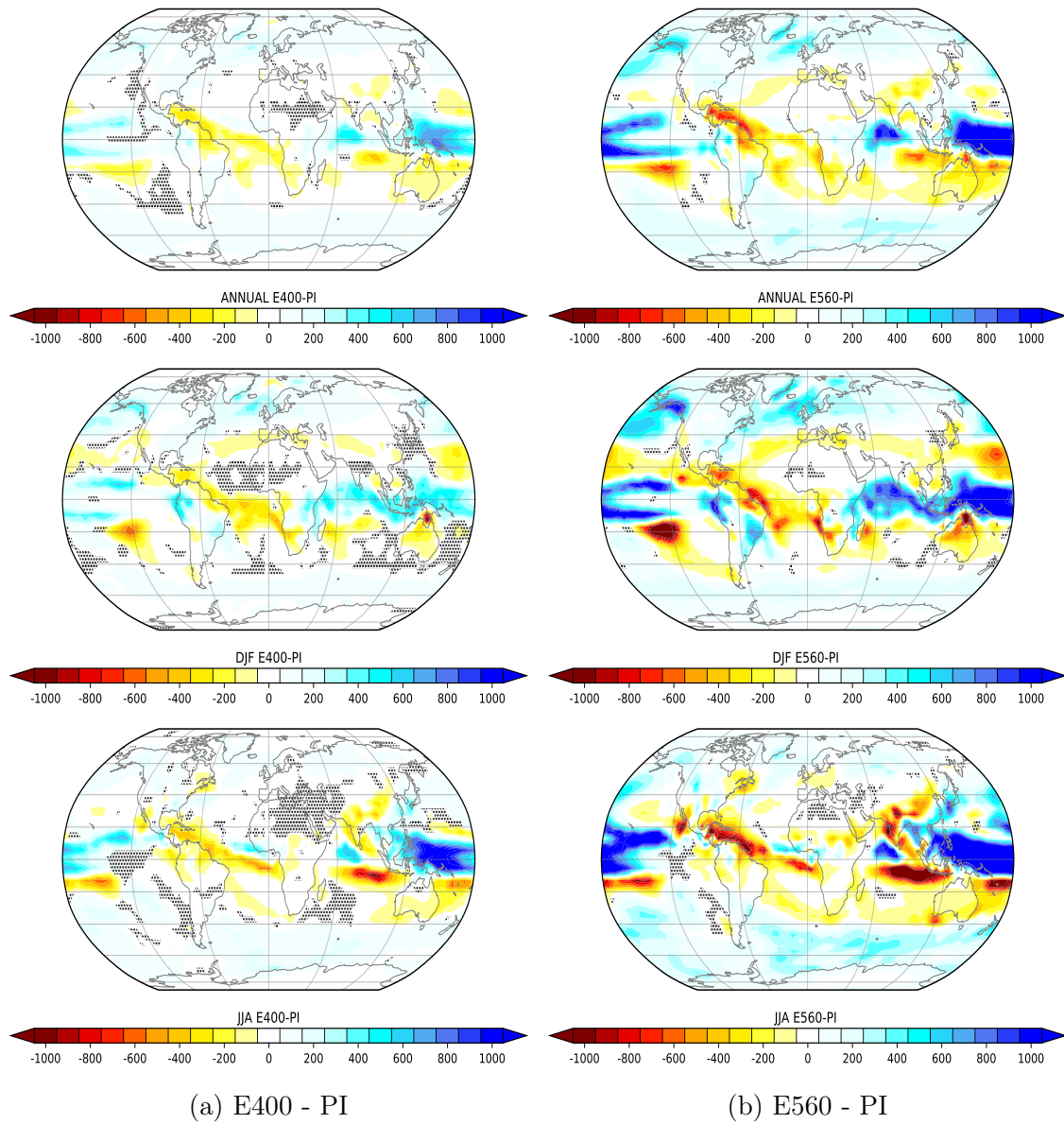


Figure 3.8: Precipitation anomaly for COSMOS simulations E400 minus PI (a) and E560 minus PI (b). The unit is mm/year. The hatched areas indicate regions where the anomaly is insignificant based on a t-test with 95% confidence interval.

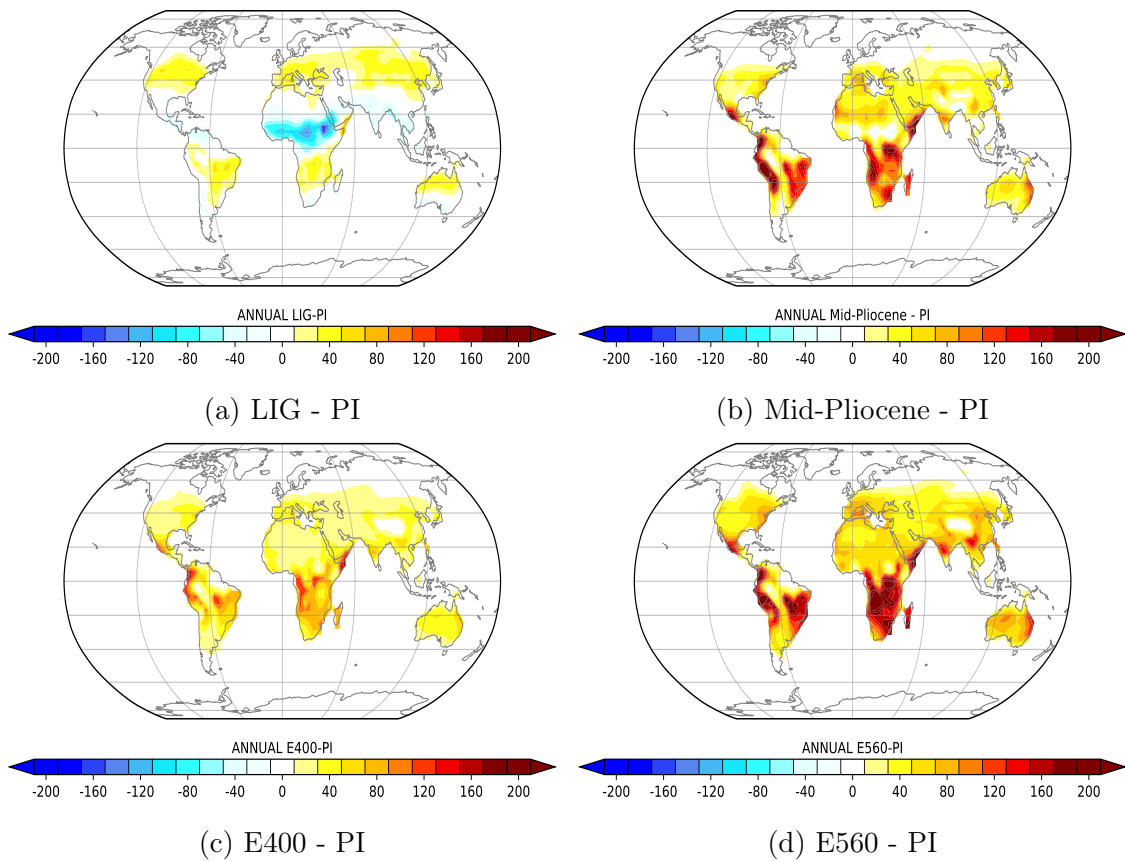


Figure 3.9: Summer days index anomaly for COSMOS simulations, LIG minus PI (a), mid-Pliocene minus PI (b), E400 minus PI (c), and E560 minus PI (d). The unit is days/year.

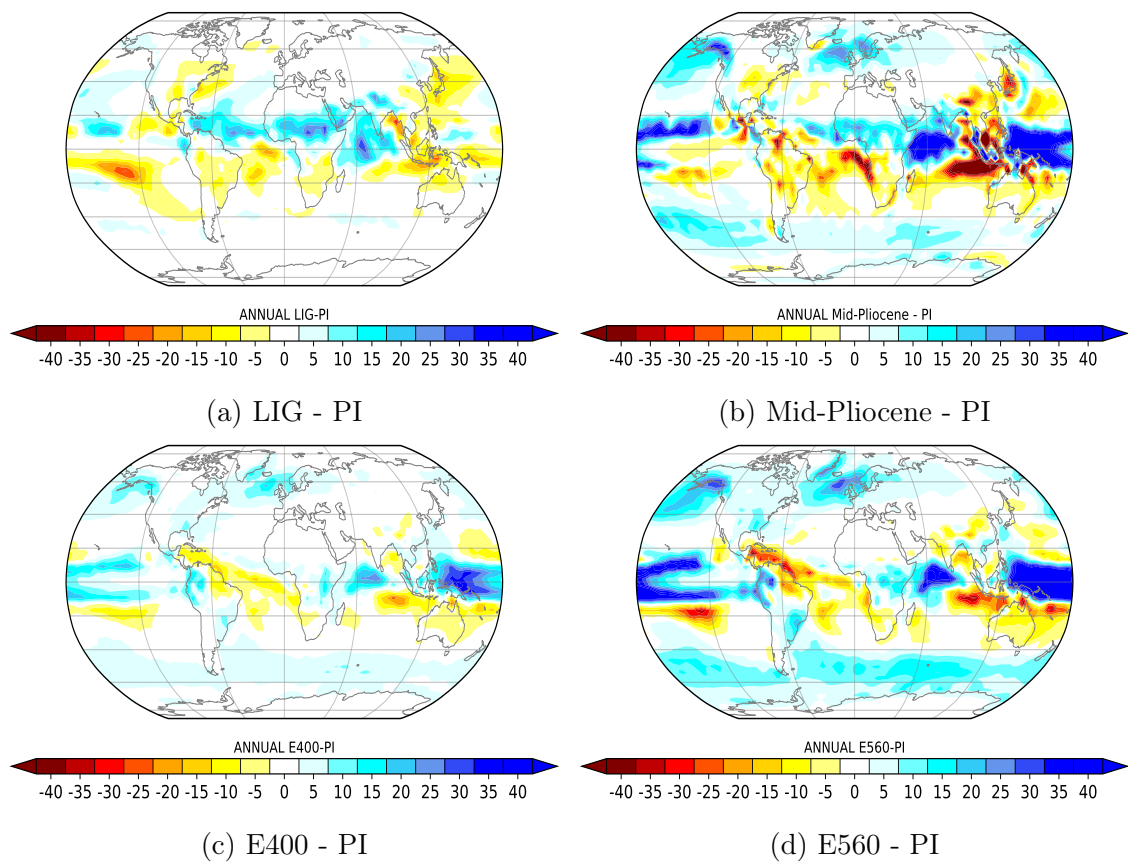


Figure 3.10: Heavy precipitation index anomaly for COSMOS simulations, LIG minus PI (a), mid-Pliocene minus PI (b), E400 minus PI (c), and E560 minus PI (d). The unit is days/year.

Chapter 4

Climate Extremes via Analysis of PDF

In this chapter, in order to show how the changes in the average of daily temperature and precipitation result in variations in climate extreme indices (Fig. 2.4), the PDF of the summer day index, heavy precipitation index, and corresponding variable (temperature or precipitation) are produced in four areas, which are described in the following sections, for the different simulations with respect to PI. The PDF approach for comparing climate extreme indices in different periods has been chosen by [Alexander et al. \(2006\)](#), [Russo and Sterl \(2011\)](#), and [Frich et al. \(2002\)](#). The choice of regions is based on the global anomaly plots of extreme indices (Fig. 3.10, Fig. 3.4, Fig. 3.9, and Fig. 3.3). Indices are averaged over the chosen regions, and then PDFs are produced for each region by binning annual values of the indices for various simulations using a bin width of 1 days. However, the climate variables PDFs are plotted by binning daily values of temperature and precipitation using a bin width of 1.

4.1 MPI-ESM

The centres of North America and Africa are selected for analysis in this section. During the LIG simulation conducted by MPI-ESM, remarkable positive anomalies of summer days index and heavy precipitation index are observed over the centre

of North America and centre of Africa, respectively (Fig. 3.3a, Fig. 3.4a). Model results and observations show that over North America the heat extremes have become more intense and more frequent during the past decades and will continue in the 21st century (Meehl et al., 2000). With regard to the heavy precipitation index over Central Africa: it decreased from 1955 to 2006 (Aguilar et al., 2009). However, Harrison et al. (2019) indicate that extreme events in the wet part of Sub-Saharan, including the centre of Africa, became wetter between 1950 to 2013.

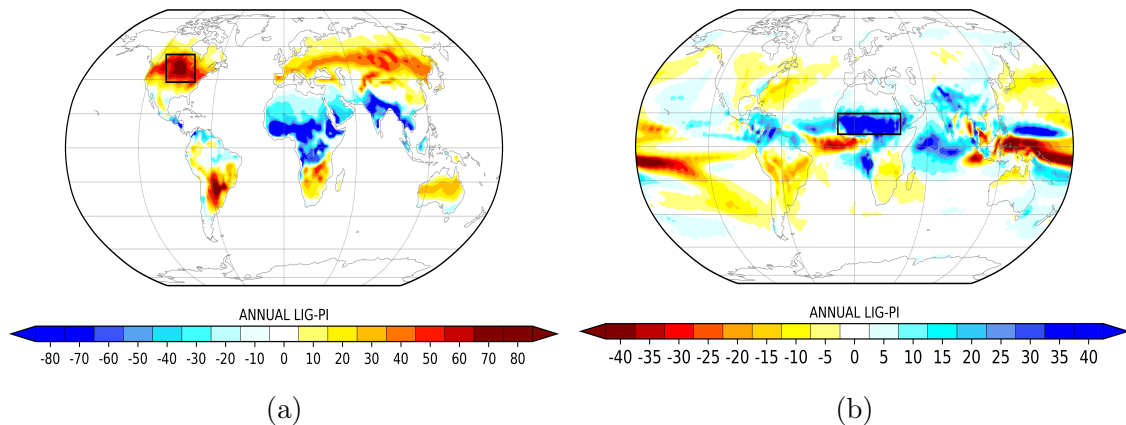


Figure 4.1: Summer days index anomaly (a) and heavy precipitation index anomaly (b) for LIG minus PI in MPI-ESM simulations. The black boxes in (a) and (b) denote the centre of North America and the centre of Africa, respectively.

Over the centre of North America, the mean temperature increases in all MPI-ESM simulations. During the LIG, the anomaly reaches its maximum in the boreal summer. In general, the temperature variation, in E400, is moderate in comparison with the LIG and E560 (Fig. 3.1). Fig. 4.2 indicates that the PDF of E560 and E400 shift towards higher temperatures, which results in a growing number of summer days in comparison with PI (Table 4.1). In the case of LIG, not only the annual mean temperature raises (Table 4.1), but also both left and right tail of the PDF is more expanded compared to PI, particularly the right tail leading to the increase of summer days (Fig. 4.2a). The annual average number of summer days in the LIG is equal to that in E560 (Table 4.1). These results illustrate that both orbital forcing and CO_2 forcing can affect the temperature extremes over the centre of North America. Moreover, the 560ppm concentration of CO_2 has an impact that is similar to orbital forcing. The significance of difference between SU density

functions (Fig. 4.2b) is tested by a two-sample Kolmogorov-Smirnov test. The D-values for LIG, E400, and E560 with regard to PI are 0.65, 0.21, and 0.52, respectively. With 95% confidence interval, the right side of the Eq. 2.7 is 0.11, therefore, the SU density functions are significantly different from PI for LIG, E400, and E560.

Table 4.1: Average of daily temperature and annual average counts of SU over the centre of North America in MPI-ESM simulations.

Simulation	Average Temperature (C°) \approx	Average SU (day/year) \approx
LIG	9.69	107
E400	9.33	81
E560	11.31	107
PI	7.86	63

During the LIG, the precipitation over the centre of Africa is strongly influenced by the monsoon rainfalls, particularly in the boreal summer. Nonetheless, this effect becomes considerably weaker in simulations E400 and E560, causing the precipitation anomalies to not significantly differ compared to PI in this region (Fig. 3.2). Table 4.2 and Fig. 4.3 denotes that the growth in the average of daily precipitation results in a noticeable increase in the extreme rainfall events in the LIG compared to other simulations. In the centre of Africa, the change in the orbital configuration of the LIG simulation is a determining factor in the occurrence of heavy precipitation events, while the concentration of CO_2 does not play a significant role. The significance of difference between R10 density functions (Fig. 4.3b) is tested by a two-sample Kolmogorov-Smirnov test. The D-values for LIG, E400, and E560 with regard to PI are 0.84, 0.02, and 0.05, respectively. With 95% confidence interval, the right side of the Eq. 2.7 is 0.11, therefore, the R10 density functions are not significantly different from PI for E400 and E560.

Table 4.2: Average of daily temperature and annual average counts of R10 over the centre of Africa in MPI-ESM simulations.

Simulation	Average Precipitation (mm/day) \approx	Average R10 (day/year) \approx
LIG	2.1	31
E400	0.2	3
E560	0.21	3
PI	0.22	3

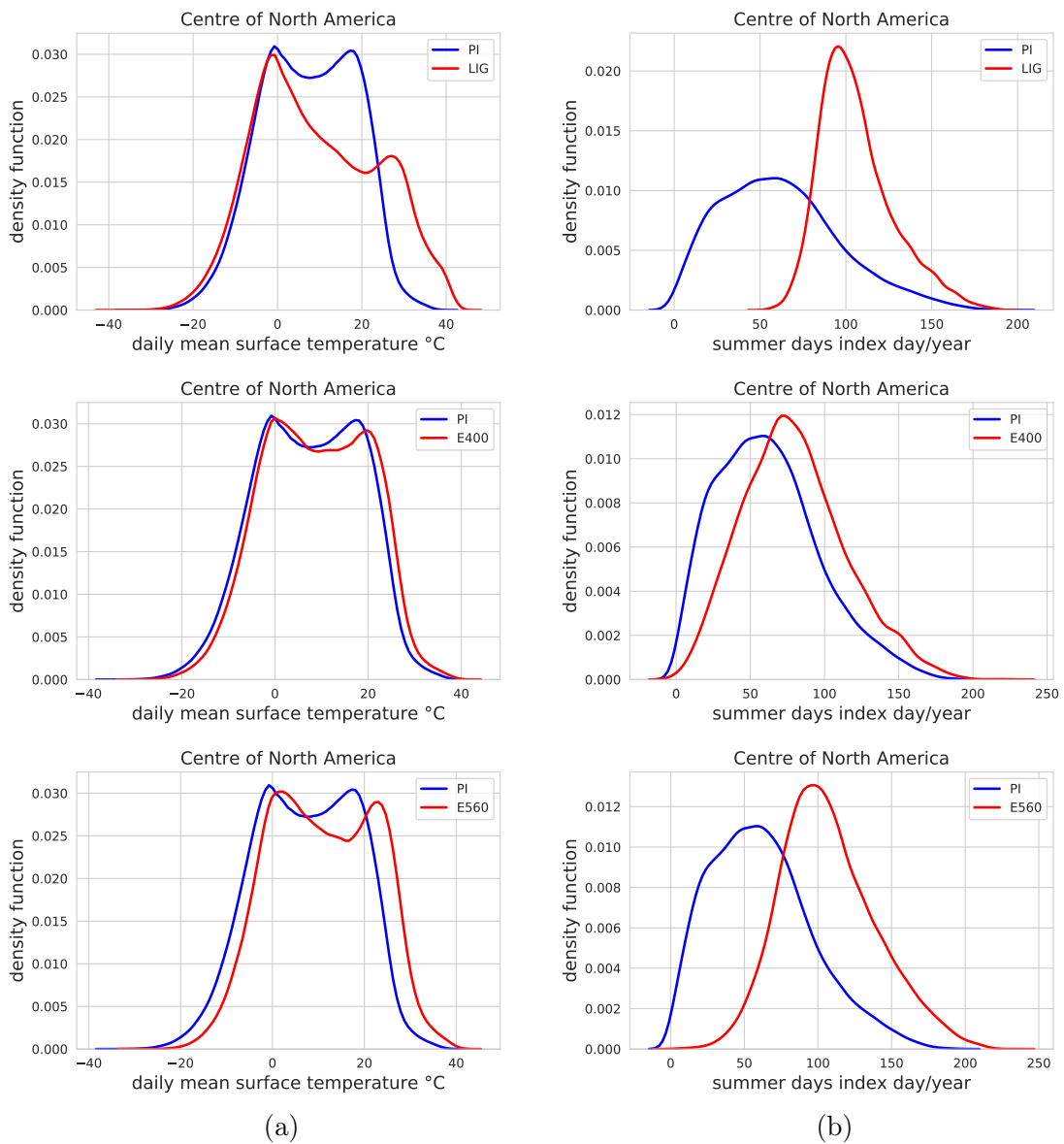


Figure 4.2: Surface temperature (a) and summer days index (b) density functions in MPI-ESM simulations for the centre of North America.

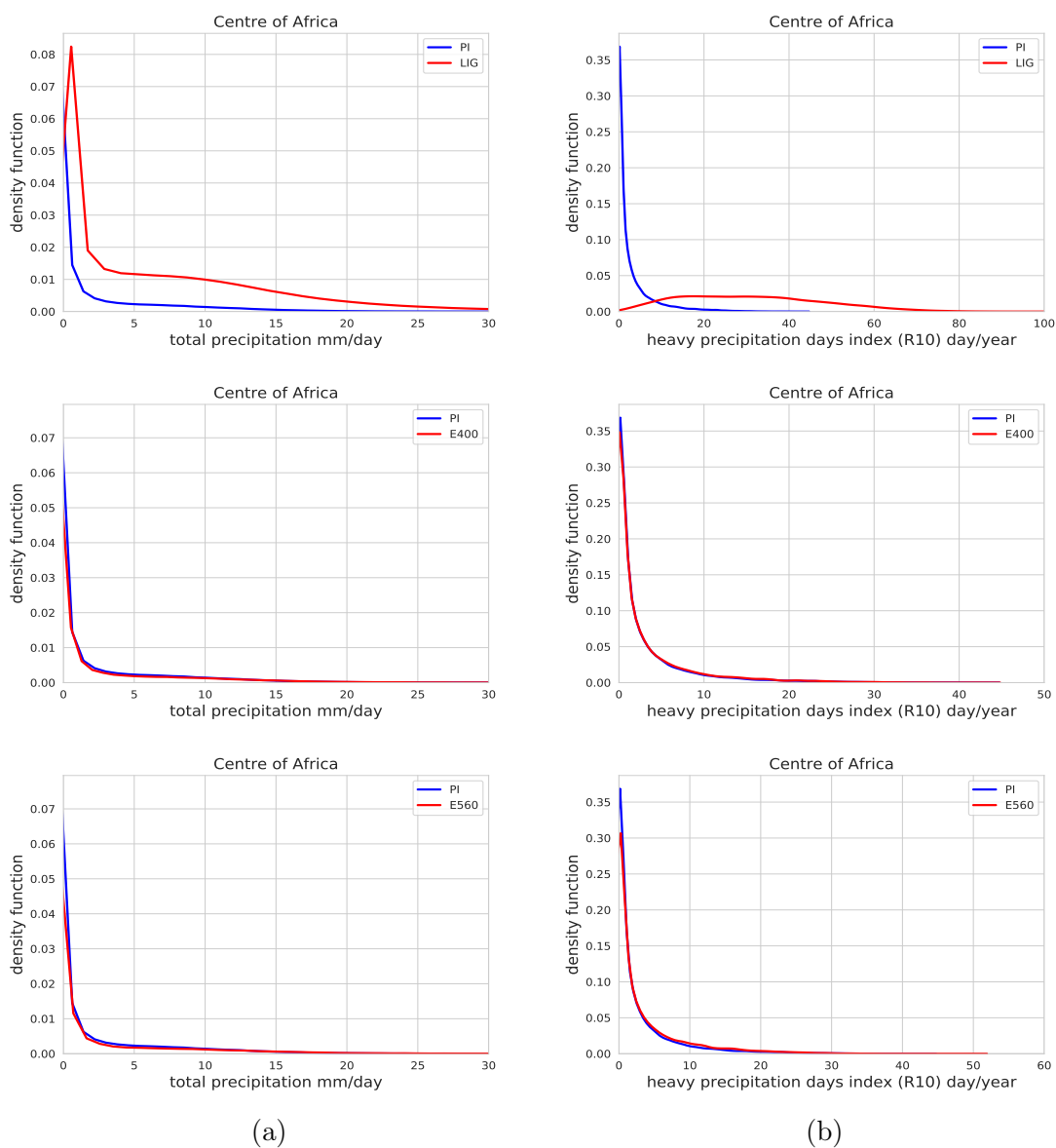


Figure 4.3: Daily precipitation (a) and R10 (b) density functions in MPI-ESM simulations for the centre of Africa.

4.2 COSMOS

Based on results presented in Fig. 3.9b and Fig. 3.10b, the South Africa and Malaysia are selected to be analyzed in the context of summer days and heavy precipitation indices, respectively. In both regions, the anomaly of the corresponding index is considerable during the mid-Pliocene simulation. The number and power of extreme heat events in the last decades (1980-2015) have increased over the south of Africa (Ceccherini et al., 2017). In general, Africa is one of the regions which will experience intense and frequent heatwaves for both future scenarios of 1.5° and 2°C global warming (Dosio et al., 2018). In Malaysia, the mean precipitation and precipitation extreme events are affected by El Niño–Southern Oscillation (ENSO) events (Tangang et al., 2017) and Southeast Asia monsoons (Endo et al., 2009). The severity and recurrence of extreme precipitation events, including heavy precipitation events, have been on the rise (Endo et al., 2009; Yik et al., 2010).

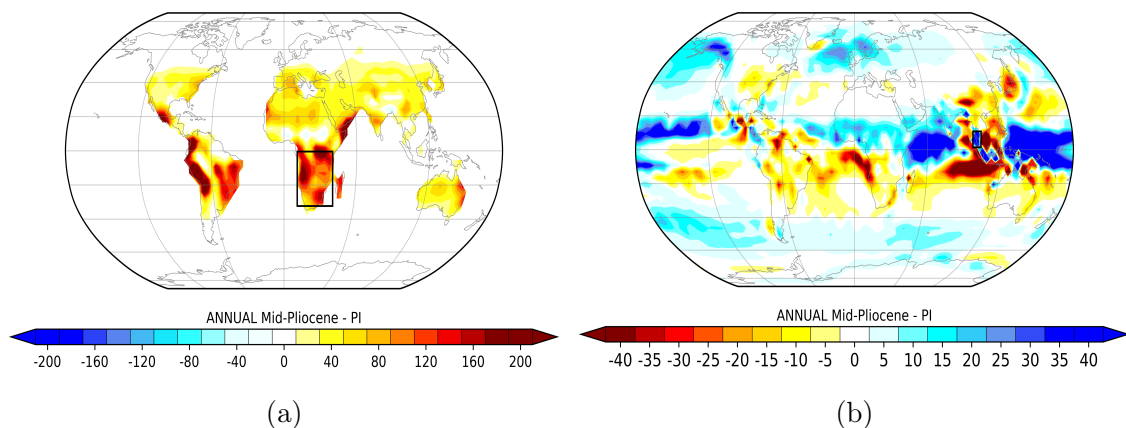


Figure 4.4: Summer days index anomaly (a) and heavy precipitation index anomaly for mid-Pliocene minus PI (b). The black box in (a) and (b) denotes the south of Africa and Malaysia, respectively.

Over the south of Africa, in all simulations, the average temperature is higher than that of PI (Fig. 3.5 and Fig. 3.6). The E560 simulation shows the highest temperature on average, and a significant shift in density function towards the right (Fig. 4.5), which causes a sizeable growth in the number of summer days (Table 4.3). In the LIG, the combination of a slight increase in temperature and skewness of the density function (Fig. 4.5) results in 29 more summer days compared to PI (Ta-

ble 3.2). The amount of atmospheric CO_2 has a significant impact on the summer days event insofar as in E560 the daily maximum temperature can almost exceed $25^\circ C$ during the whole year (Fig. 4.5, Table 4.3). The significance of difference between SU density functions (Fig. 4.5) is tested by two-sample Kolmogorov-Smirnov test. The D-values for mid-Pliocene, LIG, E400, and E560 with regard to PI is 0.54, 0.16, 0.37, and 0.76, respectively. With 95% confidence interval, the right side of the Eq. 2.7 is 0.11, therefore, the SU density functions are significantly different from PI for mid-Pliocene, LIG, E400, and E560.

Table 4.3: Average of daily temperature and annual average counts of SU over the south of Africa in COSMOS simulations.

Simulation	Average Temperature (C°) \approx	Average SU (day/year) \approx
Mid-Pliocene	25.34	251
LIG	22.12	152
E400	23.61	205
E560	26.93	307
PI	21.49	123

Over Malaysia, the annual precipitation considerably rises in the mid-Pliocene compared to PI; however, the anomalies in E400 and E560 are small, and even in the LIG, a decline in annual precipitation is observed (Fig. 3.7, Fig. 3.8). In the mid-Pliocene, the average of daily precipitation is approximately twice of that of other simulations, which ultimately leads to the largest amount of heavy precipitation events in the mid-Pliocene in this region (Table 4.4). Comparing the PDF of daily precipitation in the LIG, E400, and E560 with PI (Fig. 4.6a), it is evident that the variation in the right-tail of the functions is negligible; therefore, the annual average of heavy precipitation events does not show a considerable change in these simulations compared to PI (Fig. 4.6b, Table 4.4). These results suggest that the effect of geography- CO_2 is more pronounced than the impacts of orbital forcing and pure CO_2 forcing on extreme rainfalls over Malaysia. The significance of difference between R10 density functions (Fig. 4.6b) is tested by two-sample Kolmogorov-Smirnov test. The D-values for mid-Pliocene, LIG, E400, and E560 with regard to PI is 0.76, 0.08, 0.27, and 0.23, respectively. With 95% confidence interval, the right side of the Eq. 2.7 is 0.11, therefore, the R10 density functions are sig-

nificantly different from PI for mid-Pliocene, E400, and E560. The LIG density function, however, is not significantly different from PI.

Table 4.4: Average of daily temperature and annual average counts of R10 over Malaysia in COSMOS simulations.

Simulation	Average Precipitation (mm/day) \approx	Average R10 (day/year) \approx
Mid-Pliocene	8.09	135
LIG	4.23	66
E400	4.81	76
E560	4.58	72
PI	4.24	65

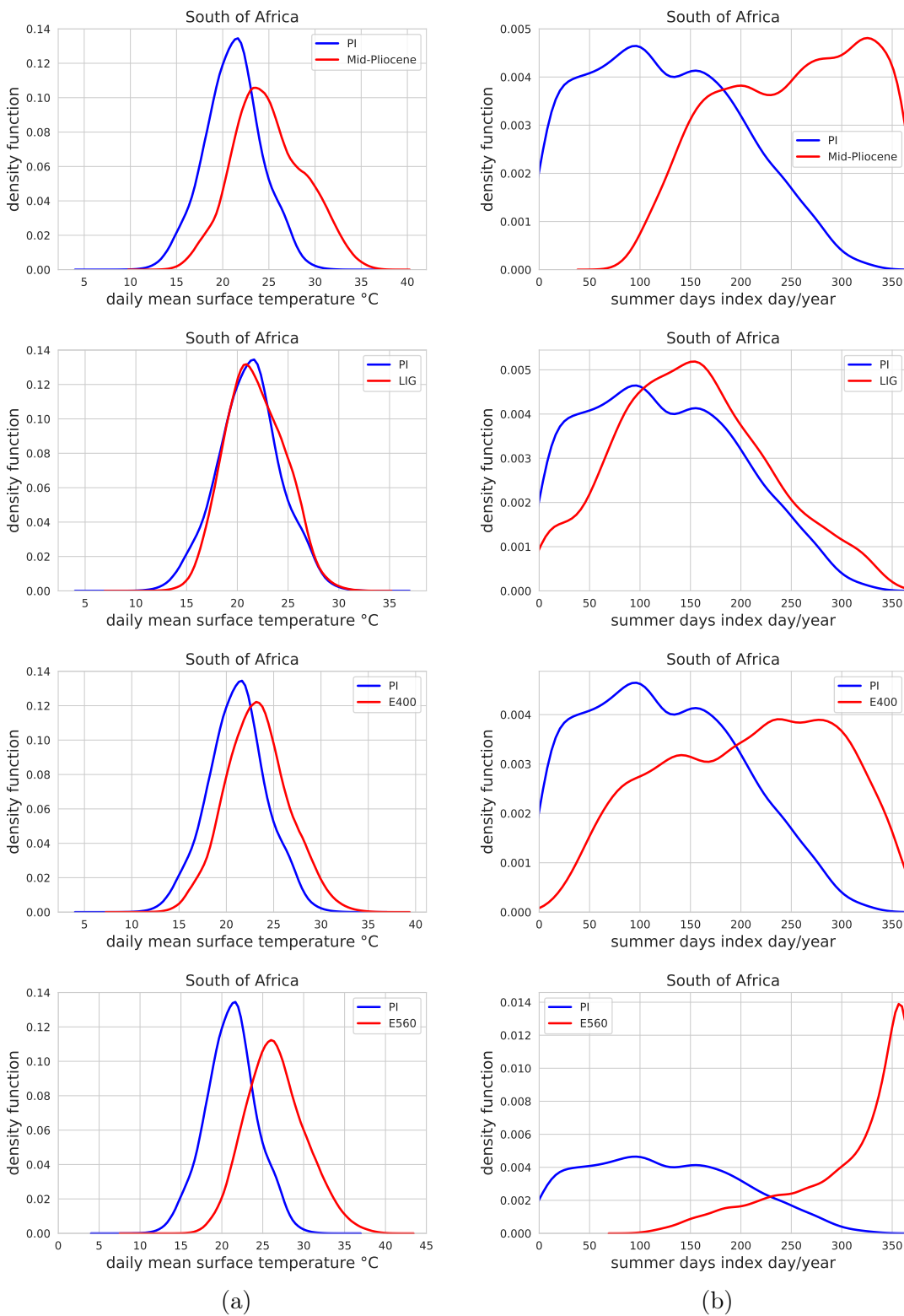


Figure 4.5: Surface temperature (a) and summer days index (b) density functions in COSMOS simulations for the south of Africa.

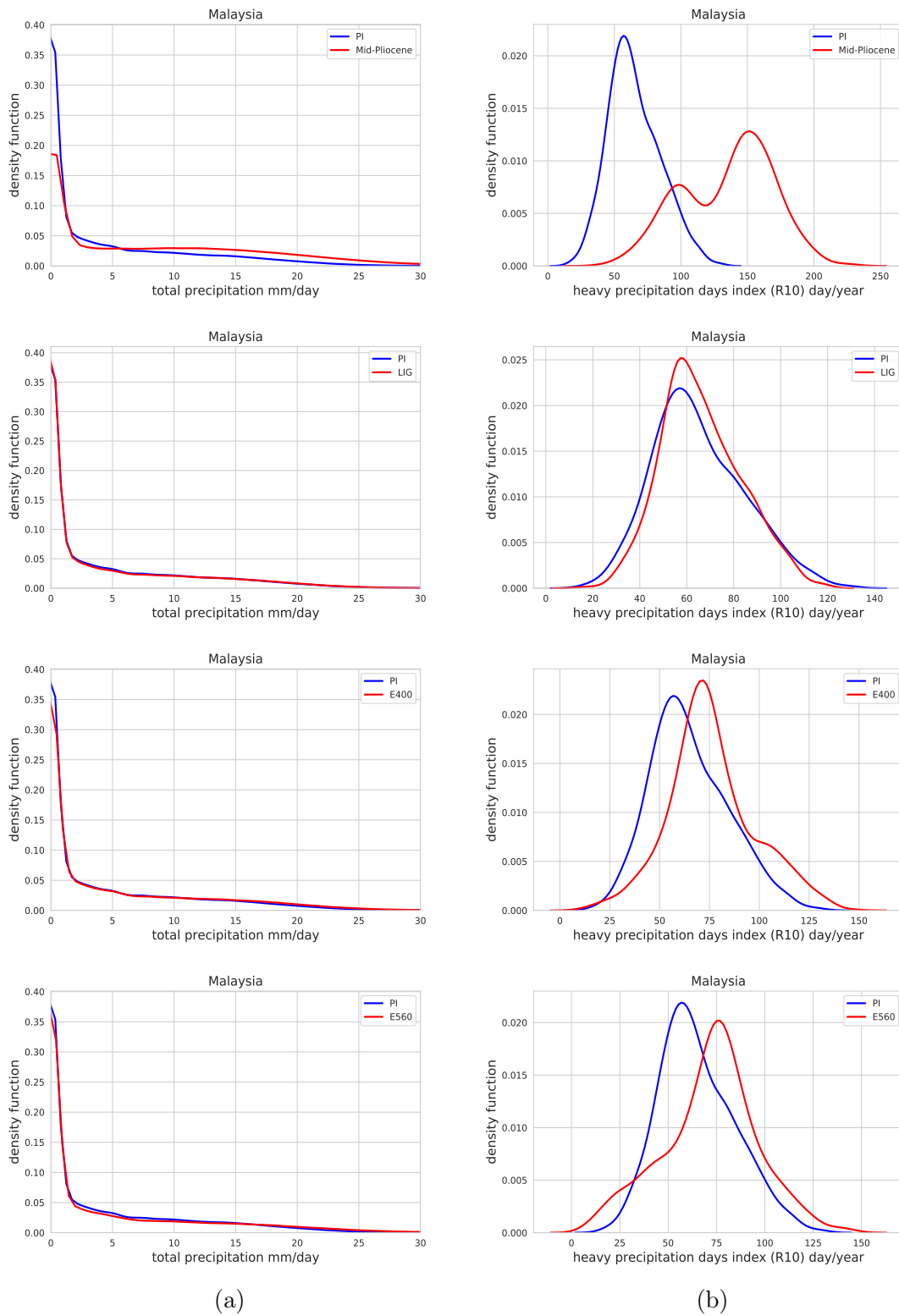


Figure 4.6: Daily precipitation (a) and R10 (b) density functions in COSMOS simulations for Malaysia.

Chapter 5

Discussion

5.1 Climate extreme indices at global scale

It is anticipated that by the end of this century, the mean global surface temperature increase by an average of 0.3°C to 4.8°C relative to 1986–2005 (Alexander et al., 2013). This ongoing warming can be intensified by higher emissions of GHGs (Alexander et al., 2013). On the other hand, the orbital driven LIG and the mid-Pliocene, the latter of which is influenced by CO_2 forcing and geography changes, are known as warmer-than-present climates (Budyko and Izrael, 1991; Raymo et al., 1996). As a consequence of rising heat energy in the atmosphere-ocean system, the frequency or intensity of extreme events increases according to the thermodynamic laws (Trenberth et al., 2015). In this thesis project, it has been shown that increases in the summer days index and heavy precipitation index are evident over many regions in the simulations compared to PI (Fig. 3.3, Fig. 3.4, Fig. 3.9, Fig. 3.10).

On the global average, the number of heavy precipitation days does not differ significantly in the simulations (Table 3.1, Table 3.2), meaning that the various forcings including orbital parameters, pure CO_2 forcing, and a combination of CO_2 and geographical changes, have the same impact on the heavy precipitation index at the global scale. However, significant regional extreme rainfall anomalies are observed in the simulations, such as over the centre of Africa in the LIG (Fig. 4.1b) and across Malaysia during the mid-Pliocene (Fig. 4.4b). Fig. 4.3 and Fig. 4.6 indicate that the rise in the average of daily precipitation in those regions results in grow

of heavy precipitation days. In general, the results imply that the heavy precipitation index should be analyzed regionally since the global average precipitation and corresponding heavy rain events do not change significantly between the different simulations.

In contrast to the heavy precipitation index, in comparison to PI, the number of summer days increases also on the global average in the simulations except for the orbitally-driven LIG simulations (Table 3.1, Table 3.2). During the LIG, the cooling effect of strong monsoons, in Africa and Asia (Fig. 3.1a, Fig. 3.5a), does not allow the summer day events to occur as much as in the mid-Pliocene, E400, and E560 compared to PI. Table 3.1 and Table 3.2 show that the global average temperature, and subsequently the summer days, rise in the mid-Pliocene, E400, and E560 compared to PI. Simulation E560 shows the largest amplification in summer days index. According to these results, the CO_2 concentration is the most influential factor for the growth of summer days. Therefore, it is expected to that more summer days will occur in the future if the upward trend of CO_2 emission continues.

Burke et al. (2018) identifies the closest paleoclimatic analogues for the near future climate based on seasonal mean temperature. This thesis project moves a step forward and shows that whether the past climates can be analogue of extreme events for the future because the changes in climate extremes directly affect the societies and are the main way by which the societies understand the climate change (Trenberth et al., 2015). The following sections illustrate whether the LIG and mid-Pliocene can be considered as analogues for the future climate in the case of heavy precipitation events and summer days index. Moreover, the results produced by MPI-ESM are compared to those generated by COSMOS.

5.2 Last Interglacial

The main difference of the LIG simulations compared to other simulations is the variation of orbital configuration because the Earth's astronomical parameters are significant in determining the LIG climate (Kutzbach et al., 1991; Crowley and Kim, 1994; Montoya et al., 2000). In general, the last interglacial climates sim-

ulations show how models can react to notable changes in astronomical forcing (Mearns et al., 2001) and also provide an opportunity to analyse the main drivers creating an interglacial climate that was warmer than the current climate (Pfeiffer and Lohmann, 2016). The LIG can also be considered as a good analogue for the high latitudes in the NH (Burke et al., 2018).

The LIG simulations show a pronounced warming during boreal summer in mid to high latitudes, particularly in the NH (Fig. 3.1a, Fig. 3.5a). This warming are also observed in the annual temperature anomaly (LIG minus PI). The increased summer insolation, caused by higher obliquity, leads to a warmer NH summer in the LIG. Fig. 3.3a and Fig. 3.9a illustrate remarkable growth in the number of summer days above 40° latitude in the NH. The cause for these increases is the rise of mean temperature. For example, over the centre of North America (Fig.4.1a), the mean temperature increases by about 2°C, resulting in a considerable growth (by around 40 days) in the number of summer days in the LIG compared to PI (Table 4.1). In this region, the LIG can be a good projection for the future of summer days index since the number of summer extreme events in E650 is equal to that during the LIG. Generally speaking, between 40° to 60° northern latitudes, the spatial distribution of summer day extremes in the LIG is similar to that in E560 (Fig. 3.3, Fig. 3.9). Table 5.1 also illustrate that the average number of summer days between these latitudes in the LIG is close to E560. About other regions, the summer days patterns should be analysed regionally. For example, there are some similarities between the LIG and E400 summer days patterns over Australia and South America (Fig. 3.3, Fig. 3.9). Consequently, the LIG can not be recognised as a good analogue for future summer day extremes at the global scale, but is a suitable candidate for regions of the NH for which the LIG has been suggested as a potential future analogue.

Table 5.1: Annual average counts of SU (day/year) between 40° and 60° in NH for the LIG and E560 simulations

Model	SU in LIG \approx	SU in E560 \approx
MPI-ESM	34	33
COSMOS	29	34

The large scale precipitation patterns are affected by atmospheric circulation determined by the meridional temperature gradients (Scussolini et al., 2019). Since the meridional temperature gradient differs in the LIG compared to E400 and E560 (Fig. 3.1), therefore, the LIG rainfall pattern is overall different (Fig. 3.2, Fig. 3.7a, Fig. 3.8). Therefore, it is difficult to find any noticeable resemblance for heavy precipitation patterns in the LIG with those in E400 and E560 (Fig.3.4, Fig. 3.10). For instance, the rise of daily mean precipitation over the centre of Africa results in sizable growth of days in which the precipitation exceeds 10 mm. In the same regions, nevertheless, in E560 and E400, the significant anomalies are not observed in both daily precipitation and heavy precipitation indices (Table 4.2, Fig. 4.3). As a result, neither locally nor globally, the LIG can be considered as an analogue for the future heavy precipitation index.

5.3 Mid-Pliocene

During the mid-Pliocene, the CO_2 concentrations have been increased with regard to PI and almost reached the modern value (400 ppm; Kürschner et al., 1996; Raymo et al., 1996; Haywood et al., 2016). Moreover, mid-Pliocene geography conditions were similar to the modern shape in many features (Jansen et al., 2007). Due to reasons above, the mid-Pliocene presents climate much warmer than present, which makes it a good analogue for the future with regard to the continuing global warming caused by excessive emissions of CO_2 (Jansen et al., 2007; Burke et al., 2018). However, there are some geographical differences in mid-Pliocene, including details in coastlines, ocean gateways, and thickness and extent of ice sheets (Dowsett et al., 2016; Haywood et al., 2016).

Table 3.2 shows that the increase of mean temperature caused by high CO_2 concentration leads to a noticeable elevation in the global number of summer days in mid-Pliocene, E400, and E560 compared to PI. There are many similarities between the summer days patterns in mid-Pliocene and E400 and E560, respectively (Fig. 3.9). Comparing Fig. 3.9b and Fig. 3.9d, the mid-Pliocene can be almost seen as a analogue for the future except for the centre of Africa because the cooling

effect of monsoon is stronger in the mid-Pliocene. All the mid-Pliocene, E400, and E560 simulations show a sizeable growth in summer days compared to PI (Fig. 4.5); however, the anomalies in E560 are generally more powerful. Furthermore, in many regions such as North America and Asia, the summer of extremes in E400 approximately increases similarly as in the mid-Pliocene (Fig. 3.9). The south of Africa (Fig. 4.4a) is an example for how the summer days index in mid-Pliocene can be globally interpreted compared to E400 and E560. The mid-Pliocene is warmer than E400 but cooler than E560; therefore, the summer extremes in the mid-Pliocene occur more often than in E400, and less often than in E560 (Table 4.3). Therefore, the mid-Pliocene may be an example for a more distant future climate with further increased CO_2 closed to E560. At the same time, it is an instance for the future world with CO_2 conditions as the present, but with a climate which reaches equilibrium. Generally speaking, since the mid-Pliocene clearly presents the elevation of temperature and summer days extremes caused mainly by CO_2 (Stepanek et al., 2020), it is worth analyzing the mid-Pliocene as a global and regional analogue for ongoing and future climates in the case of summer days index.

The predominant driver of mid-Pliocene simulation is CO_2 concentration (Stepanek et al., 2020), which leads to the similarity of the mid-Pliocene precipitation (Fig. 3.7b) and heavy precipitation patterns in many regions to those in purely CO_2 -driven simulations, especially to E560 (Fig. 3.8, Fig. 3.10). For instance, in the equatorial Pacific Ocean, the north of Europe, the North Atlantic, the Alaska Bay, and the Arabian Sea, there is a good agreement between the mid-Pliocene and E560 simulations for the extreme rainfall anomalies (Fig. 3.10). Despite these similarities, many discrepancies are also seen. Heavy precipitation anomalies are during the mid-Pliocene, stronger in the south and south-east of Asia. For example in Malaysia (Fig. 4.4b), both daily mean precipitation and the annual average of heavy precipitation indices are considerably larger than those in E400 and E560 (Table 4.4). Moreover, the heavy rain extreme events follow a different pattern in E560 and E400 compared to the mid-Pliocene in many regions such as South America, Central America, and Africa (Fig. 3.10). In conclusion, the mid-Pliocene can be employed as a local analogue for the future climate of some regions men-

tioned above, but it is certainly not a good analogue at the global scale, where precipitation is affected by other forcings, like mid-Pliocene geography.

Table 5.2: The global annual mean temperature, precipitation, SU, and R10 for similar simulations done by COSMOS and MPI-ESM.

Models	Annual mean temperature (°C)	Annual mean SU (days/year)	Annual mean precipitation (mm/year)	Annual mean R10 (days/year)
LIG				
MPI-ESM-1-2-LR	13.41	109	1045	33
COSMOS	13.81	116	1004	33
E400				
MPI-ESM-1-2-LR	15.01	137	1063	34
COSMOS	15.66	144	1037	35
E560				
MPI-ESM-1-2-LR	16.51	154	1089	35
COSMOS	18.21	170	1088	37
PI				
MPI-ESM-1-2-LR	13.53	116	1035	32
COSMOS	13.51	116	995	33

5.4 MPI-ESM vs COSMOS

The results are represented in a new order in appendix A to have a convenient comparison between similar simulations done by COSMOS and MPI-ESM. The illustration of temperature anomalies in appendix A show that the COSMOS simulations represent higher warming compared to the MPI-ESM simulations. For example, the polar amplification during the LIG is more pronounced for COSMOS compared to MPI-ESM (Fig. A.1). Similarly, E560 simulated by COSMOS presents a warmer climate than E560 computed by MPI-ESM (Fig. A.3). Furthermore, Table 5.2 indicates that also the global mean temperature in the COSMOS simulations are higher than those in the MPI-ESM simulations, except for PI. In addition, differences in regional distribution and amount of precipitation are also observed between similar simulations done by COSMOS and MPI-ESM (Fig. A.5, Fig. A.6, Fig. A.7). Since the temperature and precipitation patterns differ between COSMOS and MPI-ESM, therefore, the distributions and intensities of summer days indices and heavy precipitation indices are not identical for similar simulations pro-

duced by these two models. With regard to the LIG simulations, the summer days anomalies are stronger in the MPI-ESM LIG simulation; however, the E400 and E560 simulations in COSMOS present more summer days than those in MPI-ESM (Fig. A.4). Fig. A.8 indicates the same pattern for heavy precipitation events as summer days index. In contrast to the LIG, the anomalies of heavy precipitation indices in E400 and E560 are larger for COSMOS.

There are several reasons for the above differences between COSMOS and MPI-ESM simulations. Regarding the E400 and E560 simulations, the main cause is that the climate sensitivity of COSMOS simulations for a doubling of CO_2 from PI conditions ($4.7^\circ C$; Stepanek et al., 2020) is larger than that of MPI-ESM simulations ($3^\circ C$; Otto-Bliesner et al., 2017). Therefore, some regions are likely more influenced by CO_2 forcing in the E560 simulation produced by E560. For examples, more global warming, particularly over the high latitudes, is observed in the COSMOS E560 (Fig. A.3); South America and Africa experience more summer days in the COSMOS simulation of E560 and E400 compared to similar simulations for MPI-ESM (Fig. A.4); in contrast to the future simulation done by MPI-ESM, the COSMOS E560 show negative anomalies over India and Australia (Fig. A.7); finally, the anomalies of heavy precipitation index (Fig. A.8) are more pronounced in the COSMOS E560 and E400 simulations compared to similar simulations in MPI-ESM. Moreover, the heavy rain events reduce over Australia in E560 and E400 simulated by COSMOS, while it slightly decreases in the similar simulations in MPI-ESM (Fig. A.8).

The climate sensitivity is likely not the cause for differences between orbitally-driven LIG simulations because the CO_2 concentrations in these simulations are similar to PI. The LIG simulations are probably more influenced by other model characteristics such as resolution. The model resolution, which is particularly important for the simulation of precipitation (Iorio et al., 2004), is higher for MPI-ESM (Sec. 2.1) compared to the COSMOS (Sec. 2.2). In general, the MPI-ESM LIG simulation shows more powerful precipitation anomalies (Fig. A.5) compared to the COSMOS LIG. The India and the centre of Africa are the regions strongly affected by the model resolutions. These regions experience more precipitation (Fig. A.5) and

heavy rain events (Fig. A.8) during the MPI-ESM LIG simulation. Due to higher amounts of precipitation, a cooler LIG climate is simulated by MPI-ESM over the India and Sahel compared to the COSMOS LIG simulation (Fig. A.1). Furthermore, the summer days event occurred over the India and south of Asia during the MPI-ESM LIG are less than those in the COSMOS LIG simulation (Fig. A.4). In conclusion, MPI-ESM is suggested for the simulation of LIG climate in comparison with COSMOS.

In addition, there is also a slight difference in the solar constant between MPI-ESM and COSMOS. The solar constant in MPI-ESM simulations is $1360.747 \text{ W.m}^{-2}$ (Table 2.1), while the solar constant in COSMOS is 1367 W.m^{-2} (Table 2.2). Moreover, the radiation scheme in ECHAM6 used in MPI-ESM has been improved compared to ECHAM5 employed in COSMOS (Stevens et al., 2013). The significant improvements include representation of solar radiation, surface albedo, the middle atmosphere as part of the standard model, and new description of the aerosols (Stevens et al., 2013). The combination of the mentioned differences between COSMOS and MPI-ESM cause that the temperature and precipitation patterns, and subsequently the summer days and heavy precipitation indices, regionally and globally differ for the similar simulations done by COSMOS and MPI-ESM.

Chapter 6

Conclusions

The large climate changes expected for the coming decades will occur at a significantly accelerated pace compared with Cenozoic (from 65.5 million years ago to present day) climate change and across a considerably more fragmented landscape, rife with additional stresses (Burke et al., 2018). The rates of temperature increases expected this century are at the high end of those recorded in geological history (Lovejoy, 2006). According to thermodynamic laws, increasing heat energy in the atmosphere-ocean system is anticipated to raise the frequency or intensity of extreme events (Trenberth et al., 2015) that can have negative impacts on many human societies or distribution of other species. Moreover, acknowledging the worst scenario for CO_2 emission, the LIG is relatively a good future climate analogue for 2100 in the NH, and the mid-Pliocene can be considered as a global analogue for the future temperature (Burke et al., 2018). Based on this knowledge, this thesis has been written to show whether the LIG and mid-Pliocene are reliable analogues for climate extremes.

In this project, MPI-ESM and COSMOS were employed to simulate the climate with a different configuration, including the LIG, mid-Pliocene, PI, E400 (climate in equilibrium with 400 ppm CO_2 concentration), and E560 (climate in equilibrium with 560 ppm CO_2 concentration). The daily mean value of relevant climate parameters, temperature and total precipitation, for the LIG, mid-Pliocene, E400, and E560 simulations were compared with those of the PI. Additionally, two extreme indices, including summer day index and heavy precipitation index, were

selected, and globally and regionally, analyzed. The results have generally shown that the increase in the mean precipitation and temperature results in the rise of a corresponding extreme index; however, this relation is nonlinear. On the global average, the heavy precipitation index does not considerably change between the simulations, but the summer days index is directly affected by the growth of CO_2 concentration. The most extensive summer days amplification occurs in the E560 simulations.

This thesis has indicated that the LIG can not be an analogue for the future of summer days index at the global scale. Still, it is recommended as a regional analogue of future climate with doubling CO_2 compared to PI, for example, for the centre of North America. With regard to the heavy precipitation index, the orbitally-driven LIG, globally and regionally, can not be recognized as an analogue of future climate. Concerning the mid-Pliocene, it is a worthy simulation to be analyzed as both global and local analogue for future of summer days index. Nevertheless, the mid-Pliocene can only be used as a regional analogue for heavy precipitation index. This project has also highlighted some differences in the results calculated by MPI-ESM and COSMOS. The E400 and E560 simulations are likely influenced by climate sensitivity of models for a doubling of CO_2 from PI conditions. The more global warming and subsequently, more summer days occur in the E560 simulated by COSMOS compared to the MPI-ESM E560 simulation. Furthermore, the resolution of the models probably plays a vital role in the LIG simulations. The precipitation and heavy rain extreme anomalies in the LIG simulated by MPI-ESM are more pronounced than those in the COSMOS LIG.

Finally, in order to improve our understanding of climate extremes in the past warmer-than-present climates, the following recommendations are suggested for the future studies:

- For the study of climate extreme usually, a set of climate extreme indicators are used to cover all aspects of tails of temperature and precipitation PDF (e.g. [Alexander et al., 2006](#)). Analyzing a combination of climate extreme indices can complete the study of extremes in the past.
- The high-resolution daily data sets are essential for the study of climate ex-

tremes. Therefore, the high-resolution climate models are strongly recommended to produce the daily outputs of past climates.

- If possible, the comparison of model results for extremes with the proxies can determine the validity of simulated climate extreme events.

Acronyms

CDO Climate Data Operator.

COSMOS Community Earth System Models.

DJF December-January-February.

E400 Climate Simulation in equilibrium with 400 ppm CO_2 concentration.

E560 Climate Simulation in equilibrium with 560 ppm CO_2 concentration.

GHG Greenhouse Gases.

GRIB General Regularly-distributed Information in Binary form.

IPCC Intergovernmental Panel on Climate Change.

ITCZ Inter-Tropical Convergence Zone.

JJA June-July-August.

LIG Last Interglacial (127,000 years before present).

MPI-ESM Max-Planck-Institute Earth System Model in version MPI-ESM-1-2-LR.

NetCDF Network Common Data Form.

NH Northern Hemisphere.

PDF Probability Density Function.

PI Pre-Industrial.

R10 Heavy Precipitation Index.

SH Southern Hemisphere.

SU Summer Days Index.

Bibliography

- Aguilar, E., Aziz Barry, A., Brunet, M., Ekan, L., Fernandes, A., Massoukina, M., Mbah, J., Mhanda, A., Do Nascimento, D., Peterson, T., et al. (2009). Changes in temperature and precipitation extremes in western central africa, guinea conakry, and zimbabwe, 1955–2006. *Journal of Geophysical Research: Atmospheres*, 114(D2).
- Alexander, L., Allen, S., Bindoff, N. L., et al. (2013). Working group i contribution to the ipcc fifth assessment report climate change 2013: The physical science basis summary for policymakers. Technical report, IPCC.
- Alexander, L. V., Zhang, X., Peterson, T. C., Caesar, J., Gleason, B., Klein Tank, A., Haylock, M., Collins, D., Trewin, B., Rahimzadeh, F., et al. (2006). Global observed changes in daily climate extremes of temperature and precipitation. *Journal of Geophysical Research: Atmospheres*, 111(D5).
- Berger, A. L. (1978). Long-term variations of caloric insolation resulting from the earth's orbital elements. *Quaternary Research*, 9(2):139–167.
- Brovkin, V., Claussen, M., Driesschaert, E., Fichefet, T., Kicklighter, D., Loutre, M.-F., Matthews, H. D., Ramankutty, N., Schaeffer, M., and Sokolov, A. (2006). Biogeophysical effects of historical land cover changes simulated by six earth system models of intermediate complexity. *Climate Dynamics*, 26(6):587–600.
- Budyko, M. and Izrael, Y. (1991). Paleoclimatic evidence of climatic sensitivity to changing atmospheric gas concentration. *Anthropogenic Climate Change*, pages 279–318.
- Burke, K., Williams, J., Chandler, M., Haywood, A., Lunt, D., and Otto-Bliesner, B. (2018). Pliocene and Eocene provide best analogs for near-future climates. *Proceedings of the National Academy of Sciences*, 115(52):13288–13293.
- Ceccherini, G., Russo, S., Ameztoy, I., Marchese, A. F., and Carmona-Moreno, C. (2017). Heat waves in africa 1981-2015, observations and reanalysis. *Natural Hazards & Earth System Sciences*, 17(1).
- Chen, C.-T. and Knutson, T. (2008). On the verification and comparison of extreme rainfall indices from climate models. *Journal of Climate*, 21(7):1605–1621.
- Christensen, J. H., Carter, T. R., Rummukainen, M., and Amanatidis, G. (2007). Evaluating the performance and utility of regional climate models: the prudence project.
- Council, N. R. (1999). *Global environmental change: Research pathways for the next decade*. National Academies Press, Washington, DC.

- Cronin, T. M., Whatley, R., Wood, A., Tsukagoshi, A., Ikeya, N., Brouwers, E., and Briggs Jr, W. (1993). Microfaunal evidence for elevated pliocene temperatures in the arctic ocean. *Paleoceanography*, 8(2):161–173.
- Crowley, T. J. and Kim, K.-Y. (1994). Milankovitch forcing of the last interglacial sea level. *Science*, 265(5178):1566–1568.
- de los Milagros Skansi, M., Brunet, M., Sigró, J., Aguilar, E., Groening, J. A. A., Bentancur, O. J., Geier, Y. R. C., Amaya, R. L. C., Jácome, H., Ramos, A. M., et al. (2013). Warming and wetting signals emerging from analysis of changes in climate extreme indices over south america. *Global and Planetary Change*, 100:295–307.
- DeConto, R. M. and Pollard, D. (2016). Contribution of antarctica to past and future sea-level rise. *Nature*, 531(7596):591–597.
- Dosio, A., Mentaschi, L., Fischer, E. M., and Wyser, K. (2018). Extreme heat waves under 1.5 c and 2 c global warming. *Environmental Research Letters*, 13(5):054006.
- Dowsett, H., Dolan, A., Rowley, D., Moucha, R., Forte, A. M., Mitrovica, J. X., Pound, M., Salzmann, U., Robinson, M., Chandler, M., et al. (2016). The prism4 (mid-piacenzian) paleoenvironmental reconstruction. *Climate of the Past*, 12(7):1519–1538.
- Dutton, A., Webster, J. M., Zwartz, D., Lambeck, K., and Wohlfarth, B. (2015). Tropical tales of polar ice: evidence of last interglacial polar ice sheet retreat recorded by fossil reefs of the granitic seychelles islands. *Quaternary Science Reviews*, 107:182–196.
- Easterling, D. R., Kunkel, K. E., Wehner, M. F., and Sun, L. (2016). Detection and attribution of climate extremes in the observed record. *Weather and Climate Extremes*, 11:17–27.
- Endo, N., Matsumoto, J., and Lwin, T. (2009). Trends in precipitation extremes over southeast asia. *Sola*, 5:168–171.
- Eyring, V., Bony, S., Meehl, G. A., Senior, C. A., Stevens, B., Stouffer, R. J., and Taylor, K. E. (2016). Overview of the coupled model intercomparison project phase 6 (CMIP6) experimental design and organization. *Geoscientific Model Development*, 9(5):1937–1958.
- Fischer, E. M. and Schär, C. (2009). Future changes in daily summer temperature variability: driving processes and role for temperature extremes. *Climate Dynamics*, 33(7-8):917.
- Frich, P., Alexander, L. V., Della-Marta, P., Gleason, B., Haylock, M., Tank, A. K., and Peterson, T. (2002). Observed coherent changes in climatic extremes during the second half of the twentieth century. *Climate research*, 19(3):193–212.
- Giorgetta, M. A., Jungclaus, J., Reick, C. H., Legutke, S., Bader, J., Böttinger, M., Brovkin, V., Crueger, T., Esch, M., Fieg, K., et al. (2013). Climate and carbon cycle changes from 1850 to 2100 in mpi-esm simulations for the coupled model intercomparison project phase 5. *Journal of Advances in Modeling Earth Systems*, 5(3):572–597.
- Giorgi, F., Hewitson, B., Arritt, R., Gutowski, W., Knutson, T., Landsea, C., et al. (2001). Regional climate information—evaluation and projections.

- Goldner, A., Herold, N., and Huber, M. (2014). The challenge of simulating the warmth of the mid-miocene climatic optimum in cesm1. *Climate of the Past*.
- Harrison, L., Funk, C., and Peterson, P. (2019). Identifying changing precipitation extremes in sub-saharan africa with gauge and satellite products. *Environmental Research Letters*, 14(8):085007.
- Harrison, S. P., Kutzbach, J. E., Prentice, I. C., Behling, P. J., and Sykes, M. T. (1995). The response of northern hemisphere extratropical climate and vegetation to orbitally induced changes in insolation during the last interglaciation. *Quaternary Research*, 43(2):174–184.
- Hays, J. D., Imbrie, J., Shackleton, N. J., et al. (1976). Variations in the earth’s orbit: pacemaker of the ice ages. *Science*, 194(4270):1121–1132.
- Haywood, A., Dowsett, H., Dolan, A., Rowley, D., Abe-Ouchi, A., Otto-Bliesner, B., Chandler, M., Hunter, S., Lunt, D., Pound, M., et al. (2016). The pliocene model intercomparison project (pliomip) phase 2: scientific objectives and experimental design. *Climate of the Past*, 12(3):663–675.
- Houghton, E. (1996). *Climate change 1995: The science of climate change: contribution of working group I to the second assessment report of the Intergovernmental Panel on Climate Change*, volume 2. Cambridge University Press.
- Houghton, J. (2001). *Climate change 2001: The scientific basis*.
- Howell, F. W., Haywood, A. M., Otto-Bliesner, B. L., Bragg, F., Chan, W.-L., Chandler, M. A., Contoux, C., Kamae, Y., Abe-Ouchi, A., Rosenbloom, N. A., et al. (2016). Arctic sea ice simulation in the pliomip ensemble. *Climate of the Past*, 12(3):749–767.
- Iorio, J., Duffy, P., Govindasamy, B., Thompson, S., Khairoutdinov, M., and Randall, D. (2004). Effects of model resolution and subgrid-scale physics on the simulation of precipitation in the continental united states. *Climate Dynamics*, 23(3-4):243–258.
- Jansen, E., Overpeck, J., Briffa, K., Duplessy, J., Joos, F., Masson-Delmotte, V., Olago, D., Otto-Bliesner, B., Peltier, W., Rahmstorf, S., et al. (2007). Paleoclimate. *Climate change 2007: the physical science basis; contribution of Working Group I to the Fourth Assessment Report of the Intergovernmental Panel on Climate Change*.
- Jenouvrier, S., Péron, C., and Weimerskirch, H. (2015). Extreme climate events and individual heterogeneity shape life-history traits and population dynamics. *Ecological Monographs*, 85(4):605–624.
- Jungclaus, J. H., Lorenz, S., Timmreck, C., Reick, C., Brovkin, V., Six, K., Segschneider, J., Giorgetta, M., Crowley, T., Pongratz, J., et al. (2010). Climate and carbon-cycle variability over the last millennium. *Climate of the Past*, 6(5):723–737.
- Klein Tank, A. and Können, G. (2003). Trends in indices of daily temperature and precipitation extremes in europe, 1946–99. *Journal of climate*, 16(22):3665–3680.
- Klein Tank, A., Wijngaard, J., Können, G., Böhm, R., Demarée, G., Gocheva, A., Mileta, M., Pashiardis, S., Hejkrlik, L., Kern-Hansen, C., et al. (2002). Daily dataset of 20th-century surface air temperature and precipitation series for the european climate assessment. *International Journal of Climatology: A Journal of the Royal Meteorological Society*, 22(12):1441–1453.

- Kukla, G. J., Bender, M. L., de Beaulieu, J.-L., Bond, G., Broecker, W. S., Cleveringa, P., Gavin, J. E., Herbert, T. D., Imbrie, J., Jouzel, J., et al. (2002). Last interglacial climates. *Quaternary Research*, 58(1):2–13.
- Kürschner, W. M., van der Burgh, J., Visscher, H., and Dilcher, D. L. (1996). Oak leaves as biosensors of late neogene and early pleistocene paleoatmospheric CO₂ concentrations. *Marine Micropaleontology*, 27(1-4):299–312.
- Kutzbach, J., Gallimore, R., and Guetter, P. (1991). Sensitivity experiments on the effect of orbitally-caused insolation changes on the interglacial climate of high northern latitudes. *Quaternary International*, 10:223–229.
- Langebroek, P. and Nisancioglu, K. (2013). Simulating last interglacial climate with NorESM: role of insolation and greenhouse gases in the timing of peak warmth. *Clim. Past Discuss*, 9:444.
- Lemordant, L. and Gentine, P. (2019). Vegetation response to rising CO₂ impacts extreme temperatures. *Geophysical Research Letters*, 46(3):1383–1392.
- Lopes, R. H., Reid, I., and Hobson, P. R. (2007). The two-dimensional kolmogorov-smirnov test.
- Lovejoy, T. E. (2006). *Climate change and biodiversity*. The Energy and Resources Institute (TERI).
- Magel, R. C. and Wibowo, S. H. (1997). Comparing the powers of the wald-wolfowitz and kolmogorov-smirnov tests. *Biometrical Journal*, 39(6):665–675.
- Mearns, L., Hulme, M., Carter, T., Leemans, R., Lal, M., Whetton, P., Hay, L., Jones, R., Kittel, T., Smith, J., et al. (2001). Climate scenario development. In *Climate change 2001: the science of climate change*, pages 739–768. Cambridge University Press.
- Meehl, G. A., Karl, T., Easterling, D. R., Changnon, S., Pielke Jr, R., Changnon, D., Evans, J., Groisman, P. Y., Knutson, T. R., Kunkel, K. E., et al. (2000). An introduction to trends in extreme weather and climate events: observations, socioeconomic impacts, terrestrial ecological impacts, and model projections. *Bulletin of the American Meteorological Society*, 81(3):413–416.
- Milankovic, M., Berger, A., and Milankovic, V. (1995). *Milutin Milankovic 1879-1958: From His Autobiography with Comments by His Son, Vasko and a Preface by André Berger*. European Geophysical Society.
- Montoya, M., von Storch, H., and Crowley, T. J. (2000). Climate simulation for 125 kyr bp with a coupled ocean–atmosphere general circulation model. *Journal of Climate*, 13(6):1057–1072.
- Mueller, B. and Seneviratne, S. I. (2012). Hot days induced by precipitation deficits at the global scale. *Proceedings of the national academy of sciences*, 109(31):12398–12403.
- Nooijer, W. d., Zhang, Q., Li, Q., Zhang, Q., Li, X., Zhang, Z., Guo, C., Nisancioglu, K. H., Haywood, A. M., Tindall, J. C., et al. (2020). Evaluation of arctic warming in mid-pliocene climate simulations. *Climate of the Past Discussions*, pages 1–30.

- O'Mahony, M. (1986). *Sensory evaluation of food: statistical methods and procedures*, volume 16. CRC Press.
- Otto-Bliesner, B., Braconnot, P., Harrison, S. P., Lunt, D., Abe-Ouchi, A., Albani, S., Bartlein, P. J., Capron, E., Carlson, A. E., Dutton, A., Fischer, H., Goelzer, H., Govin, A., Haywood, A., Joos, F., LeGrande, A. N., Lipscomb, W. H., Lohmann, G., Mahowald, N., Nehrbass-Ahles, C., Pausata, F. S. R., Peterschmitt, J.-Y., Phipps, S. J., Renssen, H., and Zhang, Q. (2017). The PMIP4 contribution to CMIP6 – Part 2: Two interglacials, scientific objective and experimental design for Holocene and Last Interglacial simulations. *Geoscientific Model Development*, 10(11):3979–4003.
- Pachauri, R. and Reisinger, A. (2008). Climate change 2007. synthesis report. contribution of working groups i, ii and iii to the fourth assessment report. *Cambridge University Press, Cambridge*.
- Pfeiffer, M. and Lohmann, G. (2016). Greenland ice sheet influence on last interglacial climate: global sensitivity studies performed with an atmosphere–ocean general circulation model. *Climate of the Past*, (12):1313–1338.
- Planton, S., Déqué, M., Chauvin, F., and Terray, L. (2008). Expected impacts of climate change on extreme climate events. *Comptes Rendus Geoscience*, 340(9-10):564–574.
- Prell, W. L. and Kutzbach, J. E. (1987). Monsoon variability over the past 150,000 years. *Journal of Geophysical Research: Atmospheres*, 92(D7):8411–8425.
- Raddatz, T., Reick, C., Knorr, W., Kattge, J., Roeckner, E., Schnur, R., Schnitzler, K.-G., Wetzell, P., and Jungclauss, J. (2007). Will the tropical land biosphere dominate the climate–carbon cycle feedback during the twenty-first century? *Climate dynamics*, 29(6):565–574.
- Raymo, M., Grant, B., Horowitz, M., and Rau, G. (1996). Mid-pliocene warmth: stronger greenhouse and stronger conveyor. *Marine Micropaleontology*, 27(1-4):313–326.
- Robinson, M. M., Dowsett, H. J., and Chandler, M. A. (2008). Pliocene role in assessing future climate impacts. *Eos, Transactions American Geophysical Union*, 89(49):501–502.
- Roeckner, E., Bäuml, G., Bonaventura, L., Brokopf, R., Esch, M., Giorgetta, M., Hagemann, S., Kirchner, I., Kornbluh, L., Manzini, E., et al. (2003). The atmospheric general circulation model echam 5. part i: Model description.
- Russo, S. and Sterl, A. (2011). Global changes in indices describing moderate temperature extremes from the daily output of a climate model. *Journal of Geophysical Research: Atmospheres*, 116(D3).
- Schulzweida, U., Kornbluh, L., and Quast, R. (2006). Cdo user's guide. *Climate data operators, Version*, 1(6):205–209.
- Scussolini, P., Bakker, P., Guo, C., Stepanek, C., Zhang, Q., Braconnot, P., Cao, J., Guarino, M.-V., Coumou, D., Prange, M., et al. (2019). Agreement between reconstructed and modeled boreal precipitation of the last interglacial. *Science advances*, 5(11):eaax7047.

- Sillmann, J., Kharin, V. V., Zwiers, F., Zhang, X., and Bronaugh, D. (2013). Climate extremes indices in the CMIP5 multimodel ensemble: Part 2. Future climate projections. *Journal of Geophysical Research: Atmospheres*, 118(6):2473–2493.
- Stepanek, C. and Lohmann, G. (2012). Modelling mid-pliocene climate with cosmos. *Geosci. Model Dev.*, 5:1221–1243.
- Stepanek, C., Samakinwa, E., and Lohmann, G. (2020). Contribution of the coupled atmosphere–ocean–sea ice–vegetation model cosmos to the pliomip2. *Climate of the Past Discussions*, pages 1–72.
- Stevens, B., Giorgetta, M., Esch, M., Mauritsen, T., Crueger, T., Rast, S., Salzmann, M., Schmidt, H., Bader, J., Block, K., et al. (2013). Atmospheric component of the MPI-M earth system model: Echem 6. *Journal of Advances in Modeling Earth Systems*, 5(2):146–172.
- Strengers, B. J., Müller, C., Schaeffer, M., Haarsma, R. J., Severijns, C., Gerten, D., Schaphoff, S., van den Houdt, R., and Oostenrijk, R. (2010). Assessing 20th century climate–vegetation feedbacks of land-use change and natural vegetation dynamics in a fully coupled vegetation–climate model. *International Journal of Climatology*, 30(13):2055–2065.
- Tangang, F., Farzanmanesh, R., Mirzaei, A., Salimun, E., Jamaluddin, A. F., and Juneng, L. (2017). Characteristics of precipitation extremes in malaysia associated with el niño and la niña events. *International Journal of Climatology*, 37:696–716.
- Trenberth, K. E., Fasullo, J. T., and Shepherd, T. G. (2015). Attribution of climate extreme events. *Nature Climate Change*, 5(8):725–730.
- Tschumi, J. and Stauffer, B. (2000). Reconstructing past atmospheric CO₂ concentration based on ice-core analyses: open questions due to in situ production of CO₂ in the ice. *Journal of Glaciology*, 46(152):45–53.
- Vogel, M. M., Orth, R., Cheruy, F., Hagemann, S., Lorenz, R., van den Hurk, B. J., and Seneviratne, S. I. (2017). Regional amplification of projected changes in extreme temperatures strongly controlled by soil moisture-temperature feedbacks. *Geophysical Research Letters*, 44(3):1511–1519.
- Wilcox, R. R. (1997). Some practical reasons for reconsidering the kolmogorov-smirnov test. *British Journal of Mathematical and Statistical Psychology*, 50(1):9–20.
- Yik, D. J., Moten, S., Ariffin, M., and Govindan, S. S. (2010). Trends in intensity and frequency of precipitation extremes in malaysia from 1951 to 2009. *Malaysia Meteorological Department*.
- Young, I. T. (1977). Proof without prejudice: use of the kolmogorov-smirnov test for the analysis of histograms from flow systems and other sources. *Journal of Histochemistry & Cytochemistry*, 25(7):935–941.
- Zazulie, N., Rusticucci, M., and Solomon, S. (2010). Changes in climate at high southern latitudes: a unique daily record at orcadass spanning 1903–2008. *Journal of Climate*, 23(1):189–196.

- Zhang, X., Aguilar, E., Sensoy, S., Melkonyan, H., Tagiyeva, U., Ahmed, N., Kutaladze, N., Rahimzadeh, F., Taghipour, A., Hantosh, T., et al. (2005). Trends in middle east climate extreme indices from 1950 to 2003. *Journal of Geophysical Research: Atmospheres*, 110(D22).
- Zhang, X., Alexander, L., Hegerl, G. C., Jones, P., Tank, A. K., Peterson, T. C., Trewin, B., and Zwiers, F. W. (2011). Indices for monitoring changes in extremes based on daily temperature and precipitation data. *Wiley Interdisciplinary Reviews: Climate Change*, 2(6):851–870.
- Zhu, J., Poulsen, C. J., Otto-Bliesner, B. L., Liu, Z., Brady, E. C., and Noone, D. C. (2020). Simulation of early eocene water isotopes using an earth system model and its implication for past climate reconstruction. *Earth and Planetary Science Letters*, 537:116164.
- Zwiers, F. W., Alexander, L. V., Hegerl, G. C., Knutson, T. R., Kossin, J. P., Naveau, P., Nicholls, N., Schär, C., Seneviratne, S. I., and Zhang, X. (2013). Climate extremes: challenges in estimating and understanding recent changes in the frequency and intensity of extreme climate and weather events. In *Climate Science for Serving Society*, pages 339–389. Springer.

Appendix A

MPI-ESM vs COSMOS

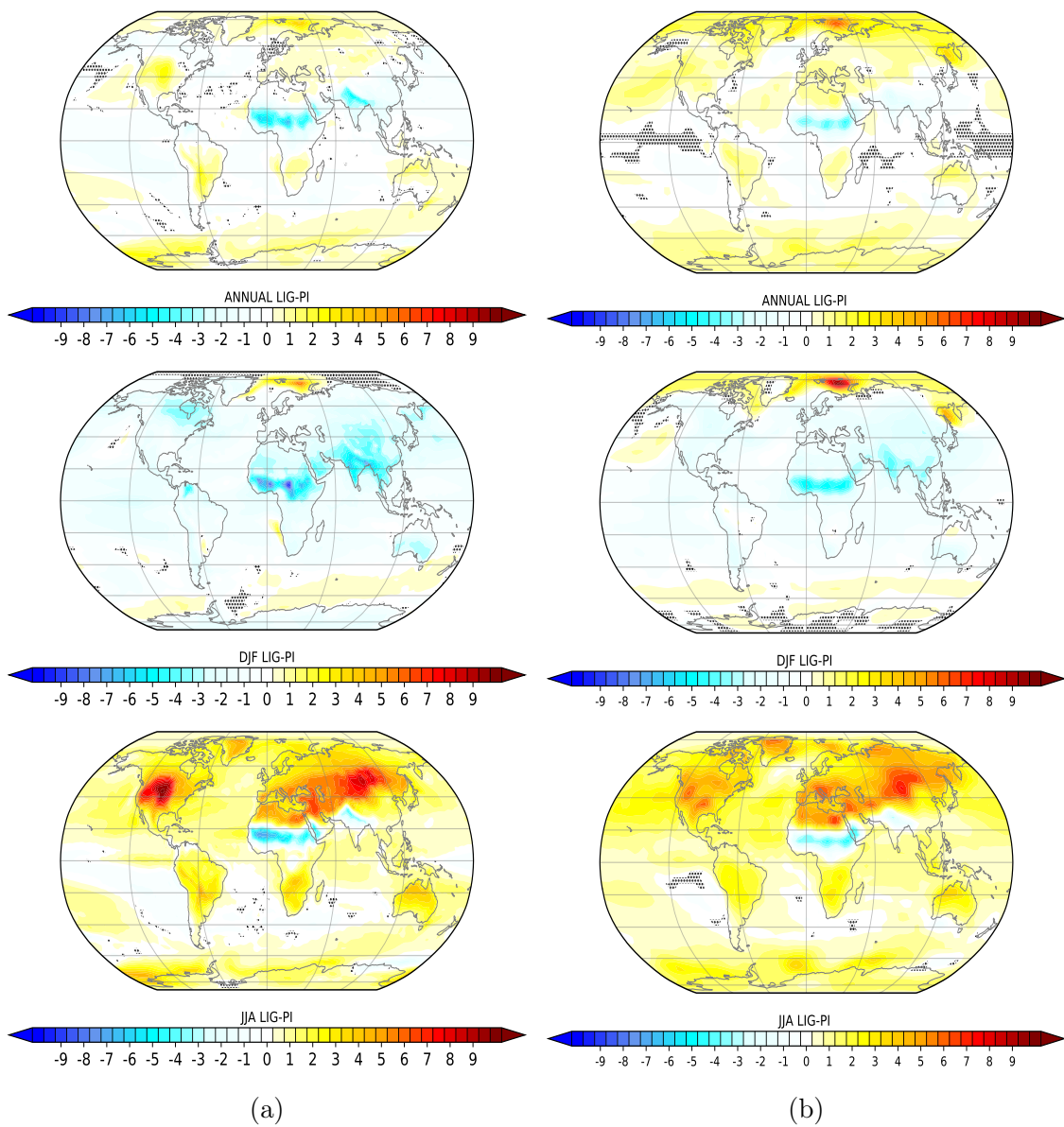


Figure A.1: Temperature anomaly for LIG minus PI simulated by MPI-ESM (a) and COSMOS (b). The unit is $^{\circ}\text{C}$. The hatched areas indicate regions in which the anomaly is insignificant based on a t-test with 95% confidence interval.

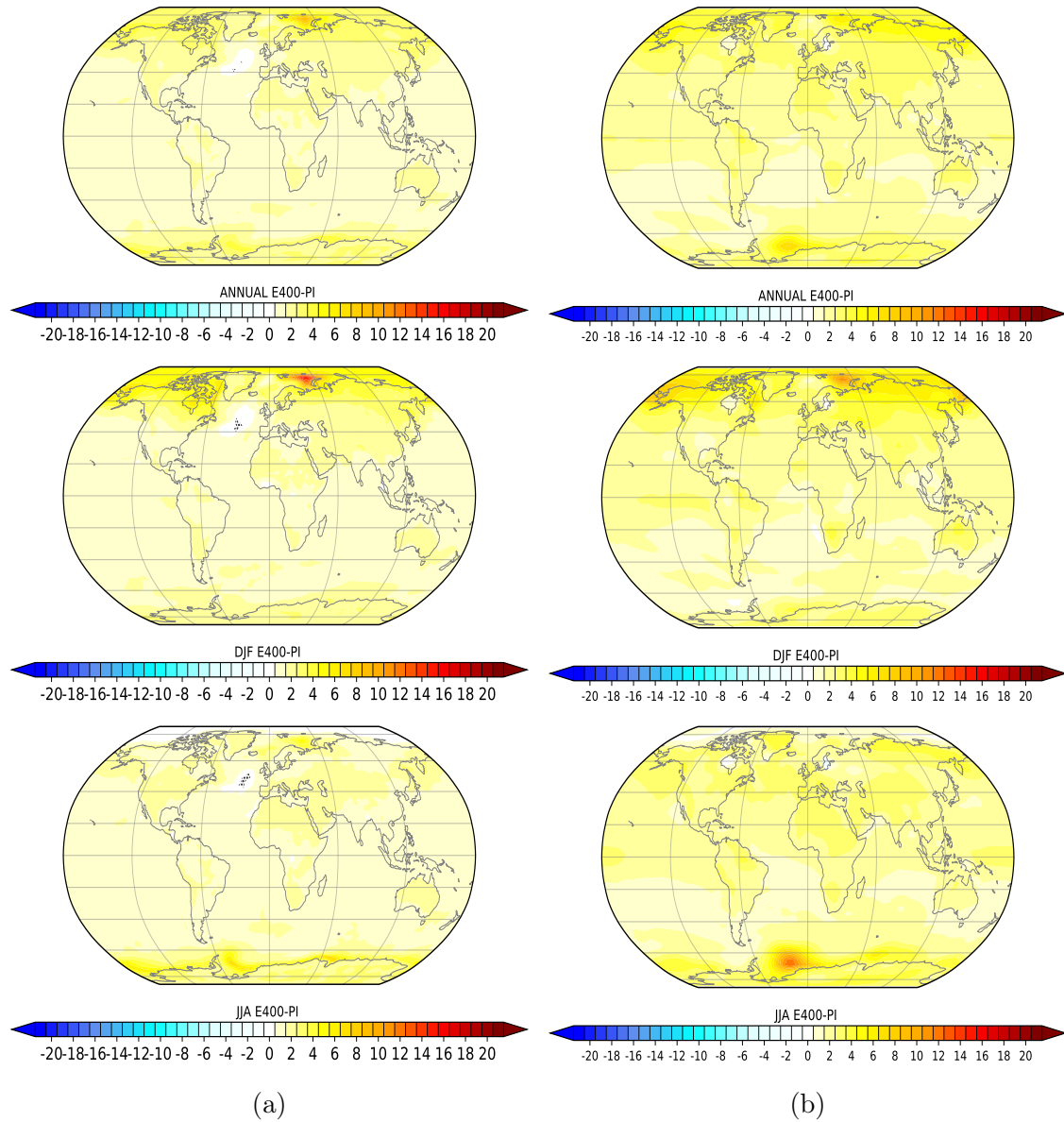


Figure A.2: Temperature anomaly for E400 minus PI simulated by MPI-ESM (a) and COSMOS (b). The unit is $^{\circ}\text{C}$. The hatched areas indicate regions in which the anomaly is insignificant based on a t-test with 95% confidence interval.

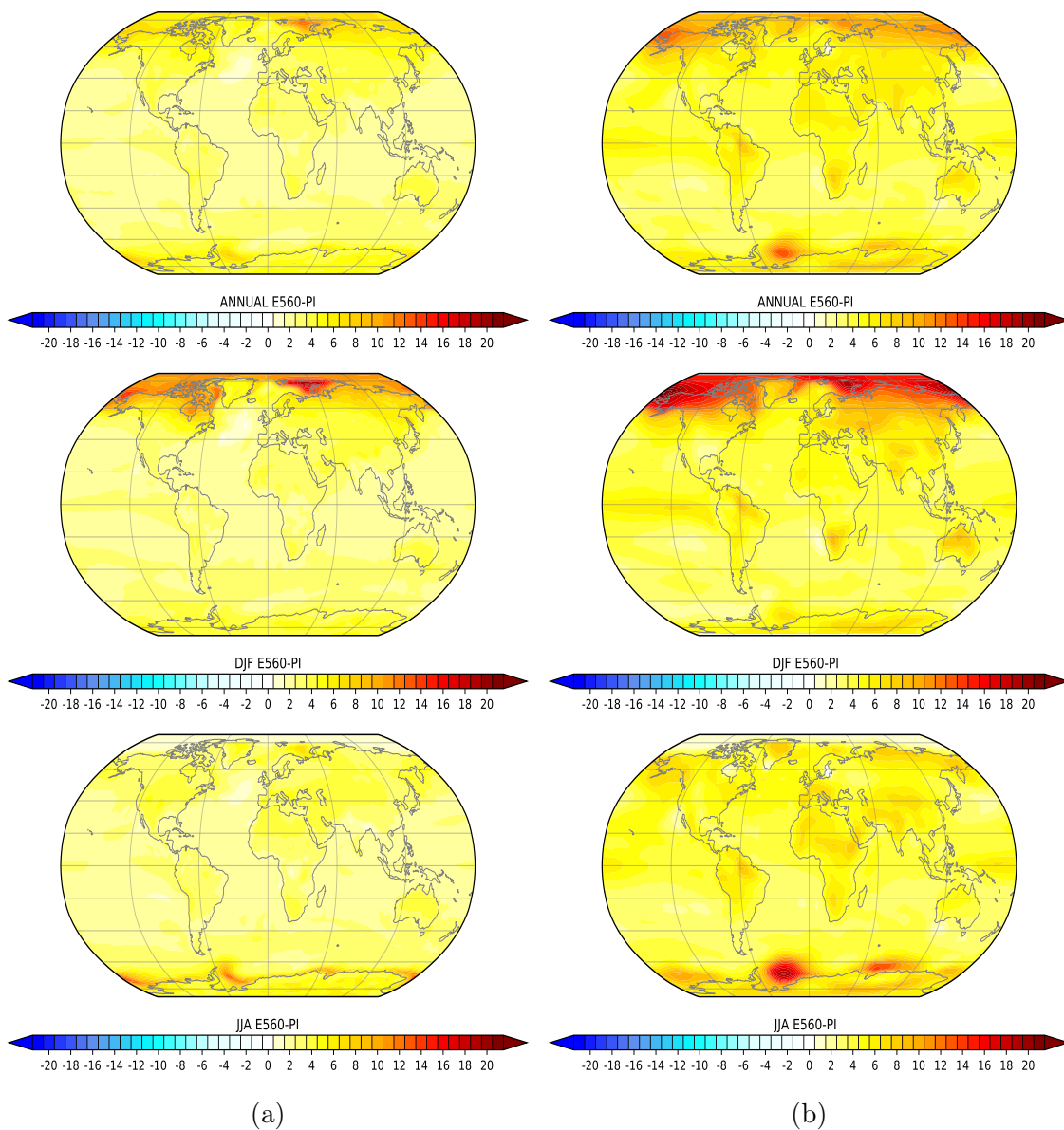


Figure A.3: Temperature anomaly for E560 minus PI simulated by MPI-ESM (a) and COSMOS (b). The unit is $^{\circ}\text{C}$. The hatched areas indicate regions in which the anomaly is insignificant based on a t-test with 95% confidence interval.

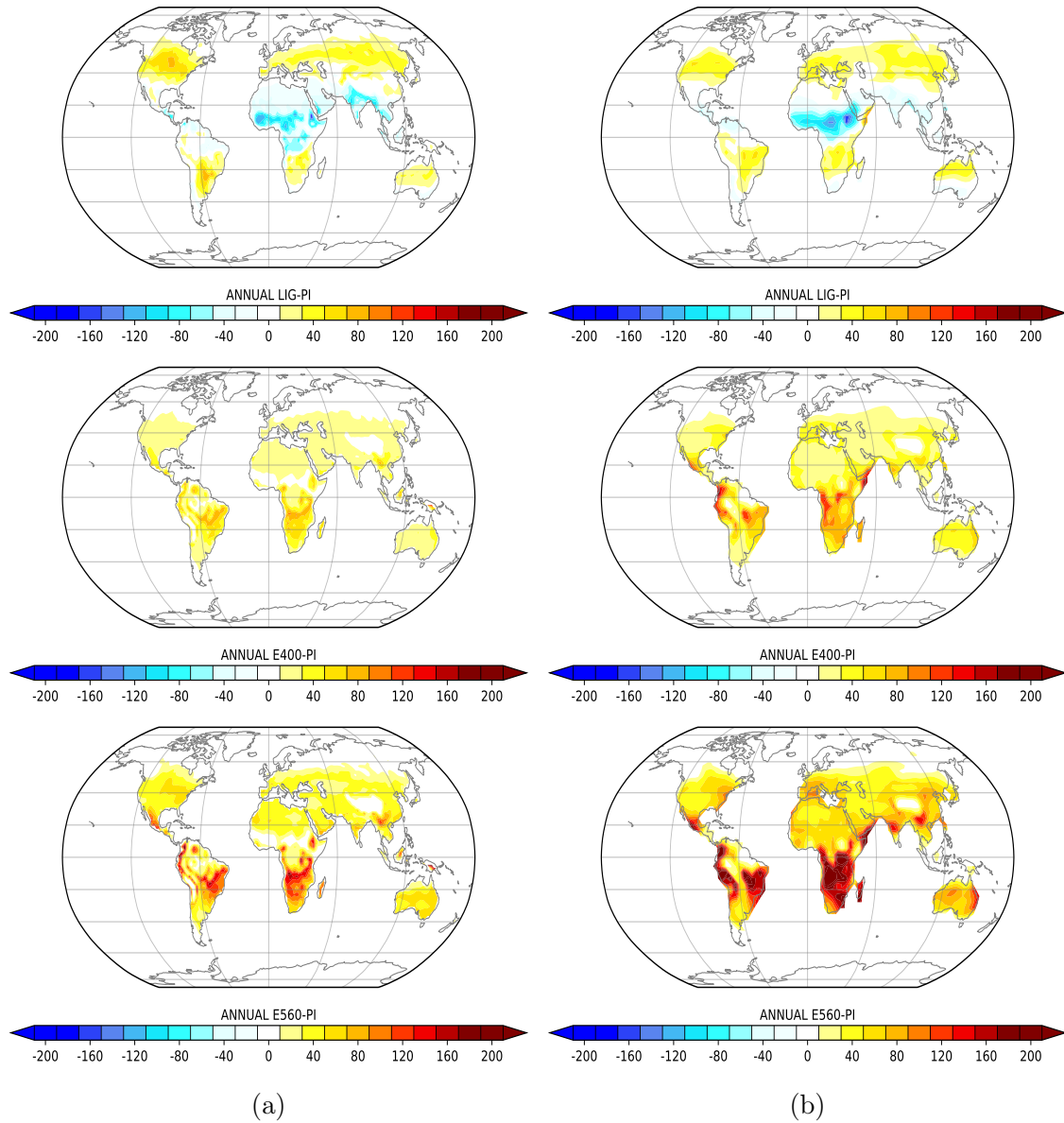


Figure A.4: Summer days anomalies for different simulations simulated by MPI-ESM (a) and COSMOS (b). The unit is day/year.

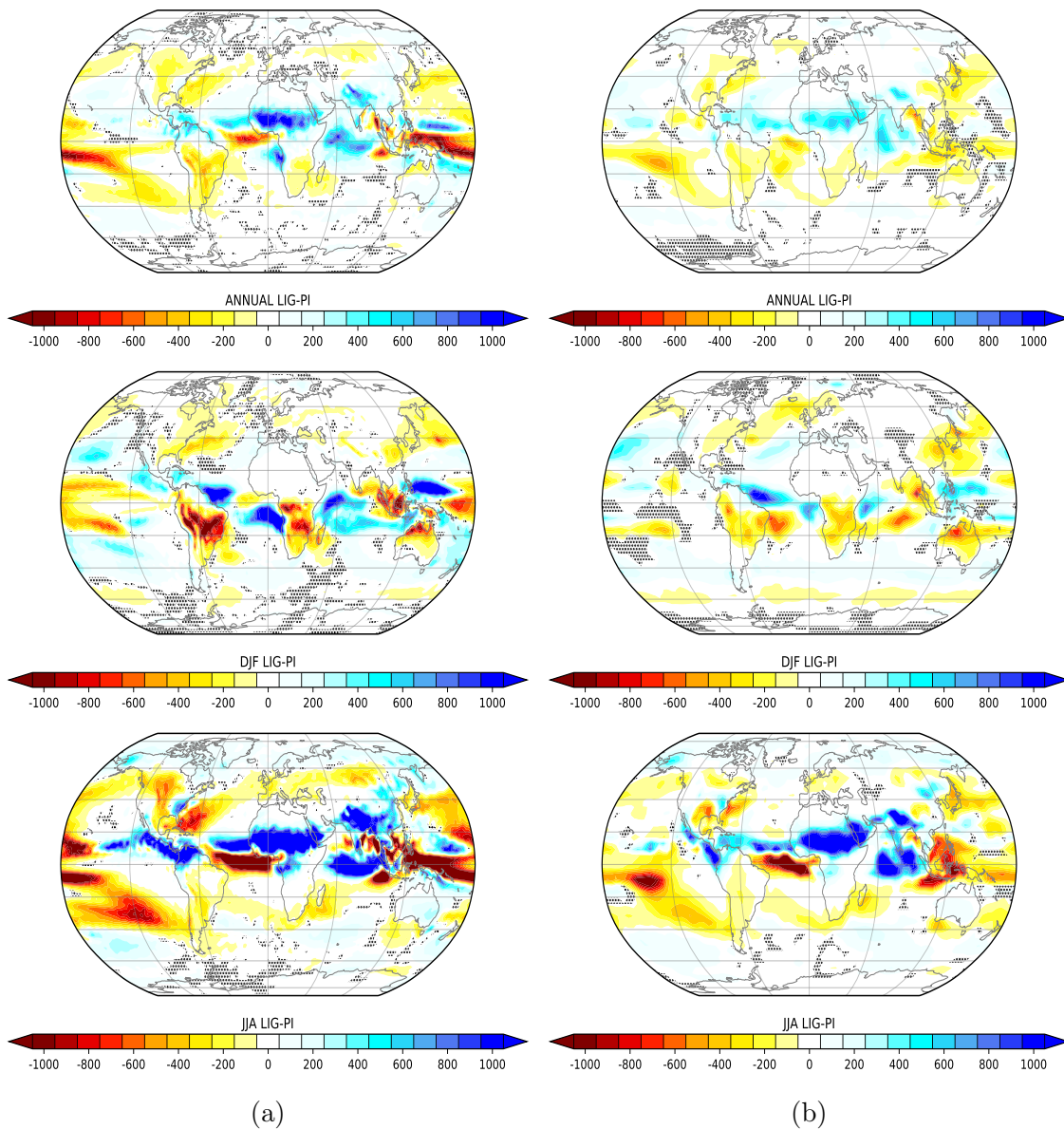


Figure A.5: Precipitation anomaly for LIG minus PI simulated by MPI-ESM (a) and COSMOS (b). The unit is mm/year. The hatched areas indicate regions in which the anomaly is insignificant based on a t-test with 95% confidence interval.

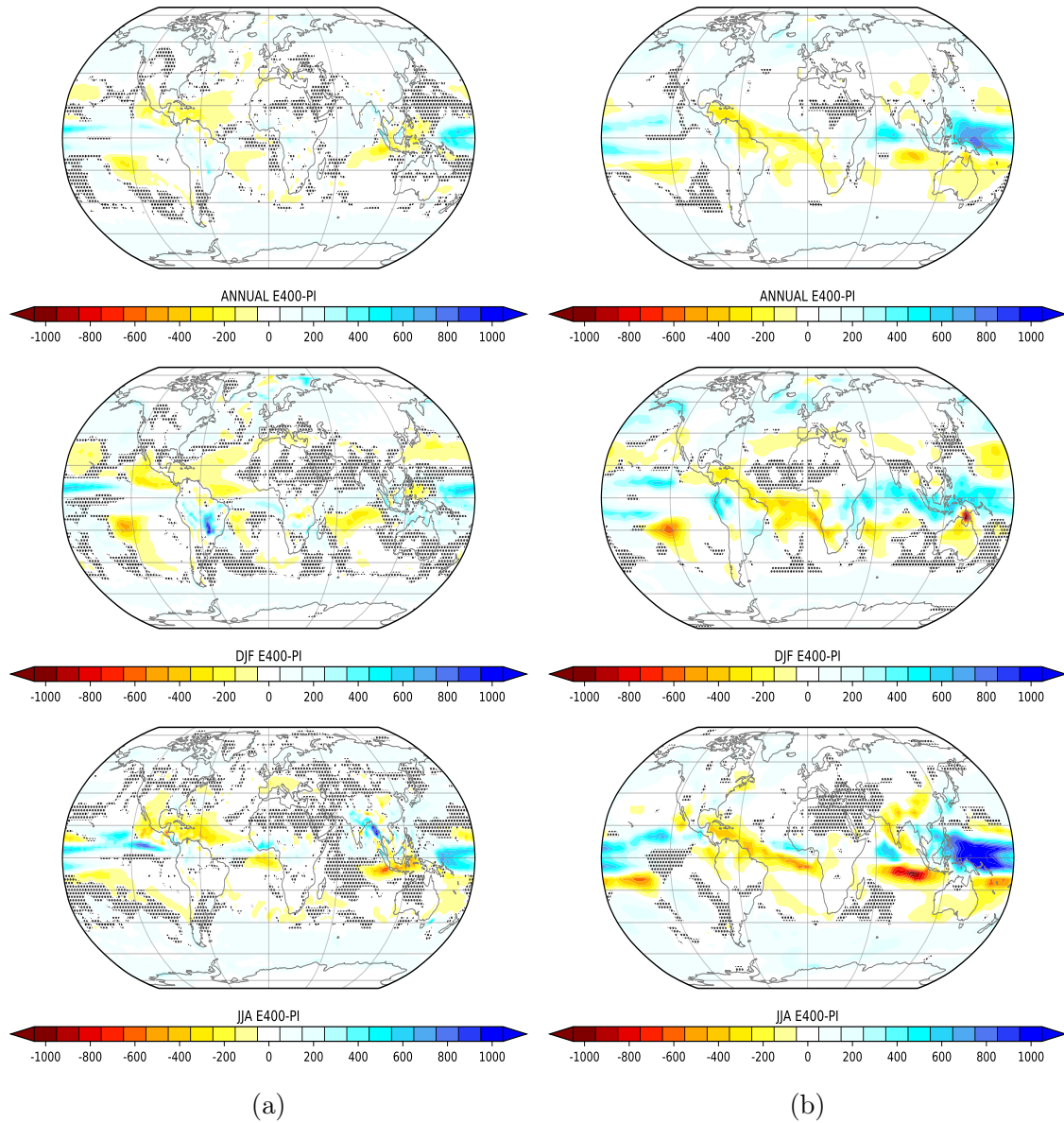


Figure A.6: Precipitation anomaly for E400 minus PI simulated by MPI-ESM (a) and COSMOS (b). The unit is mm/year. The hatched areas indicate regions in which the anomaly is insignificant based on a t-test with 95% confidence interval.

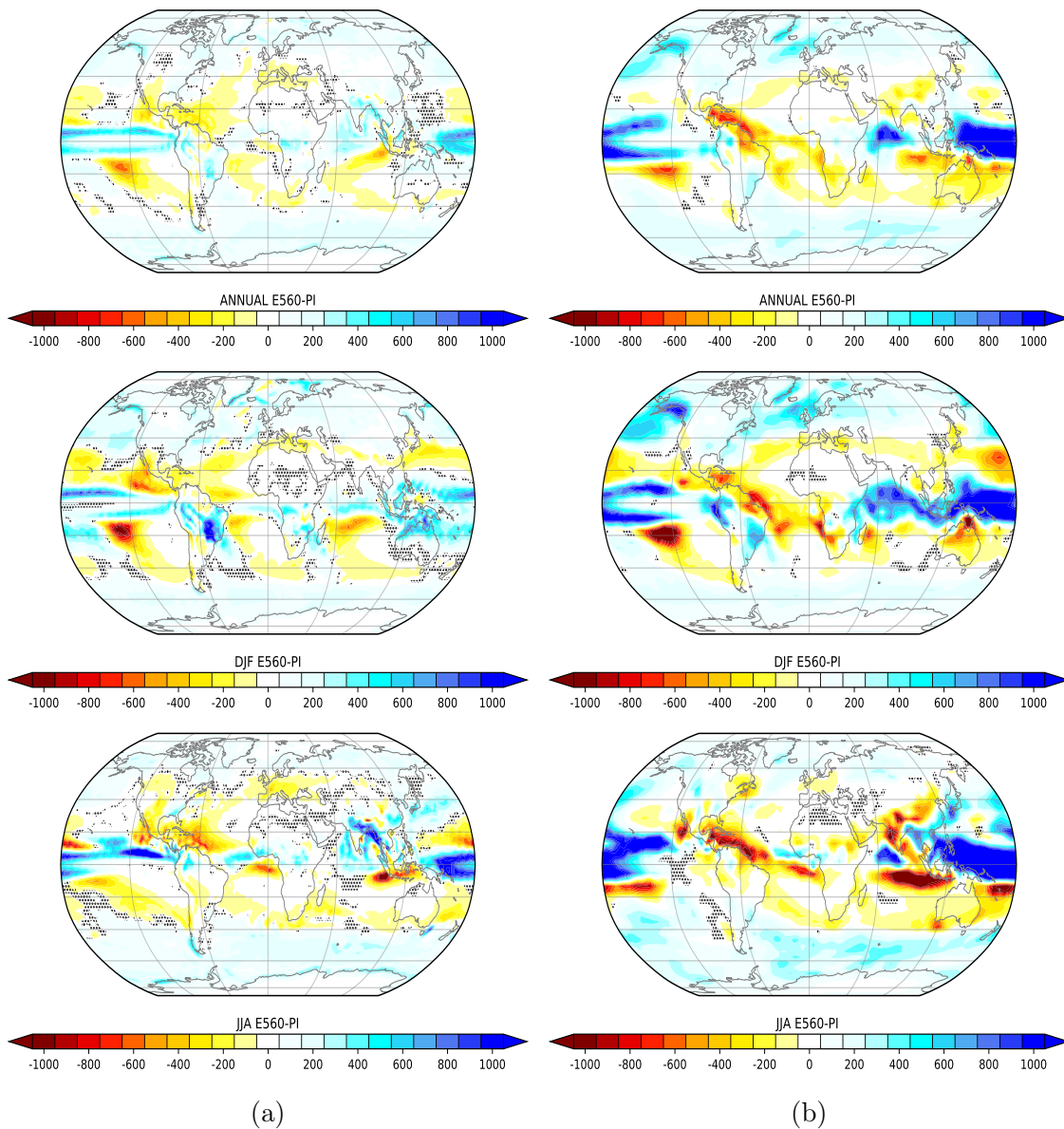


Figure A.7: Precipitation anomaly for E560 minus PI simulated by MPI-ESM (a) and COSMOS (b). The unit is mm/year. The hatched areas indicate regions in which the anomaly is insignificant based on a t-test with 95% confidence interval.

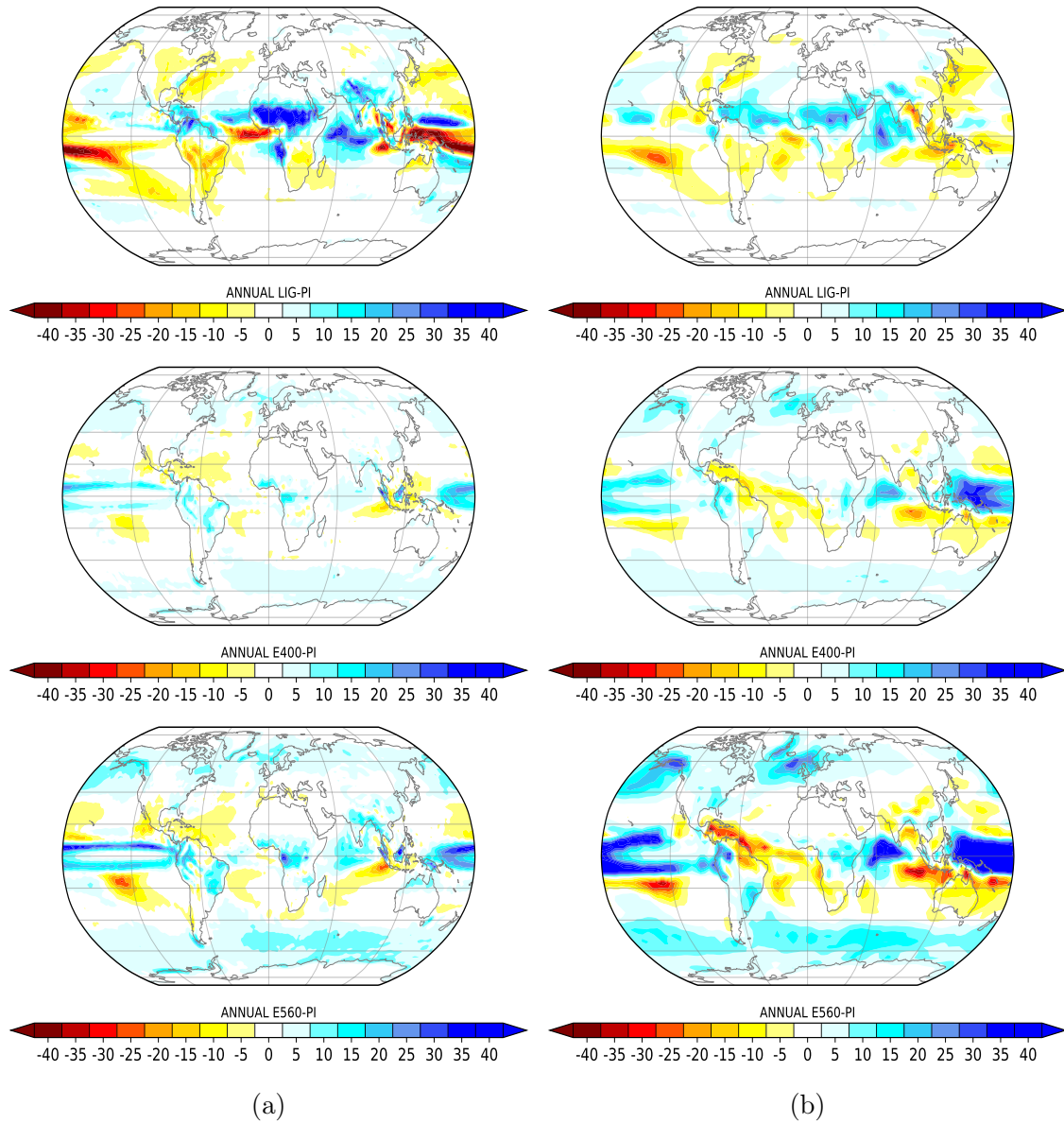


Figure A.8: Heavy precipitation anomalies for different simulations simulated by MPI-ESM (a) and COSMOS (b). The unit is day/year.